OXFORD

Cerebral Cortex, 2022, 1–20
https://doi.org/10.1093/cercor/bhac214
Original Article

Uncovering individual differences in fine-scale dynamics of functional connectivity

Sarah A. Cutts[1,2], Joshua Faskowitz[1,2], Richard F. Betzel[1,2,3,4], Olaf Sporns[1,2,3,4]*

[1]Department of Psychological and Brain Sciences, Indiana University, Bloomington, IN 47405, United States,
[2]Program in Neuroscience, Indiana University, Bloomington, IN 47405, United States,
[3]Network Science Institute, Indiana University, Bloomington, IN 47408, United States,
[4]Cognitive Science Program, Indiana University, Bloomington, IN 47405, United States

*Corresponding author: Dr. Olaf Sporns, Department of Psychological and Brain Sciences, Indiana University, Bloomington, IN, United States.
Email: osporns@indiana.edu

Functional connectivity (FC) profiles contain subject-specific features that are conserved across time and have potential to capture brain–behavior relationships. Most prior work has focused on spatial features (nodes and systems) of these FC fingerprints, computed over entire imaging sessions. We propose a method for temporally filtering FC, which allows selecting specific moments in time while also maintaining the spatial pattern of node-based activity. To this end, we leverage a recently proposed decomposition of FC into edge time series (eTS). We systematically analyze functional magnetic resonance imaging frames to define features that enhance identifiability across multiple fingerprinting metrics, similarity metrics, and data sets. Results show that these metrics characteristically vary with eTS cofluctuation amplitude, similarity of frames within a run, transition velocity, and expression of functional systems. We further show that data-driven optimization of features that maximize fingerprinting metrics isolates multiple spatial patterns of system expression at specific moments in time. Selecting just 10% of the data can yield stronger fingerprints than are obtained from the full data set. Our findings support the idea that FC fingerprints are differentially expressed across time and suggest that multiple distinct fingerprints can be identified when spatial and temporal characteristics are considered simultaneously.

Key words: functional connectivity; fMRI; resting state; connectomics.

Introduction

A key effort toward improving personalized neuroscience starts with defining which features of brain data are characteristic of individuals and how these features change across time and brain states (Mueller et al. 2013; Dubois and Adolphs 2016; Finn and Todd Constable 2016; Amico and Goñi 2018; Liu et al. 2018a; Elliott et al. 2019; Zuo et al. 2019; Gratton et al. 2020; Parkes et al. 2020). Functional connectivity (FC), a measure of correlated blood oxygen level–dependent (BOLD) activity between brain regions, is particularly suited for this task since it can capture coordinated activity across the cortex both at rest and in response to stimuli (Friston et al. 1994; Rogers et al. 2007). Using this technique, individuals can be identified from a larger group of subjects, implying there are reliable subject-specific features in FC data (Mira-Dominguez et al. 2014; Finn et al. 2015, 2017; Vanderwal et al. 2017; Waller et al. 2017; Amico and Goñi 2018; Peña-Gómez et al. 2018; Horien et al. 2019; Jalbrzikowski et al. 2020; Jo et al. 2021b). These individual specific features, referred to as "fingerprints," have already been linked to predictions of cognition (Cole et al. 2012; Rosenberg et al. 2015; Yamashita et al. 2018; Fong et al. 2019; Rosenberg et al. 2020; Sripada et al. 2020), personality (Adelstein et al. 2011; Hsu et al. 2018; Nostro et al. 2018; Dubois et al. 2018a), age (Dosenbach et al. 2010; Cabral et al. 2017; Liem et al. 2017; Nielsen et al. 2019), and disease phenotype (Lynall et al. 2010; Plitta et al. 2015; Emerson et al. 2017; Lake et al. 2019; Svaldi et al. 2021). However, distinctive variations in FC can originate from the stable functional differences between individuals, anatomical differences, within-subject variability across runs, or from differences in artifact or data acquisition (Power et al. 2012; Airan et al. 2016; Siegel et al. 2017; Bari et al. 2019; Noble et al. 2019; Botvinik-Nezer et al. 2020; Lynch et al. 2020; Noble et al. 2021). To properly compare FC between individuals or groups, stable trait-like attributes for a given task must be distinguishable from other sources of variation. Currently, the exact neurobiological bases of these fingerprints remain unclear. Isolating the specific features driving individual differences in FC patterns will be essential in determining the origins of these variations and the source of predictive qualities in functional magnetic resonance imaging (fMRI) data.

Past work has found that individual differences in FC are spatially heterogeneous and display a nonuniform distribution across time. Although it has been found that fingerprinting features are highly distributed across the cortex (Pannunzi et al. 2017; Dubois et al. 2018b; Byrge and Kennedy 2019), many individualized features seem to be concentrated within select spatial regions

Received: February 21, 2022. **Revised:** May 7, 2022. **Accepted:** May 8, 2022

such as the frontoparietal (FP), attention, and default systems (Mira-Dominguez et al. 2014; Finn et al. 2015; Airan et al. 2016; Amico and Goñi 2018; Gratton et al. 2018; Peña-Gómez et al. 2018; Ravindra et al. 2021; Sareen et al. 2021). Greater identifiability of these regions likely results from the evolutionary expansion of association cortices in humans, allowing increased phenotypic variability within areas largely "untethered" from strong developmental constraints present in conserved sensory-motor regions (Buckner and Krienen 2013; Mueller et al. 2013). Of these, many individual differences of interest to behavior are attributable to features that sufficiently differ from group shared modes of activity but are not so rare as to relate to within-subject variability or spurious connections (Amico and Goñi 2018). While these approaches consider all time points across the entire run, parallel efforts have gone toward determining both when and how specific regions or edges contribute to fingerprinting. So far, we know that subject-specificity of whole brain FC changes over time (Peña-Gómez et al. 2018), that functional networks and relation to behaviors manifest at different windowing lengths (Van De Ville et al. 2021), and that consistent states of activity patterns can be estimated for individuals across time (Vidaurre et al. 2017). These temporal approaches have focused on the dynamics of state transitions across time based on group-defined states and temporal windowing, which blurs patterns of spatial connectivity (Hindriks et al. 2016; Shakil et al. 2016; Preti et al. 2017; Esfahlani et al. 2020). Thus, most efforts so far have been unable to simultaneously pinpoint temporally and spatially precise features of subject-specific fingerprints at the resolution of single nodes and time points.

Recent work has introduced a method for decomposing FC (computed as the Pearson correlation across all time points) into moment-by-moment, single repetition time (TR) cofluctuation patterns called edge time series (eTS; Faskowitz et al. 2020). Using this technique, individualized patterns of FC appear to load onto time points with high cofluctuation amplitude, which drive full resting-state FC estimates (referred to as "events"; Esfahlani et al. 2020; Jo et al. 2021a; Betzel et al. 2022). In parallel, Sporns et al. (2021) showed that filtering the time series based on framewise similarity to bipartitioned, system-based templates yielded varying levels of individual differences for specific templates (such as cofluctuations in the FP or ventral attention [VAN] networks). While high-amplitude cofluctuations express greater subject identification than low-amplitude frames (Esfahlani et al. 2020), many of the system-based templates with high fingerprinting capability display a range of cofluctuation amplitudes that are not yet analyzed. It remains unclear how individual differences systematically vary across framewise attributes (such as cofluctuation amplitude or system template expression), what features characterize maximally identifiable moments in time, and whether there are identifiable features within FC normally obscured by high-amplitude events.

We expand on this prior work by asking: (i) Does the expression of FC fingerprints vary from moment to moment, at single TR resolution? (ii) If so, what characterizes these moments in terms of cofluctuation amplitude and functional system expression? (iii) Are the patterns found at these moments consistent across individuals and data sets? and (iv) Which features are revealed by data-driven optimization aiming to maximize subject identifiability? We show that identifiability differs systematically with cofluctuation amplitude, similarity with other frames in the run, and velocity of transitions between frames. Findings are largely consistent across different metrics of cross-subject similarity or distance and across 2 independent subject cohorts. Fingerprinting measures also varied with the level of expression of functional systems, again consistent across different metrics and subject cohorts. Lastly, we employed an optimization strategy to pinpoint both specific node sets and moments in time when subject-specific signatures of FC are maximally expressed. Optimizations converge onto 2 distinct sets of nodes in FP and VAN systems, and on specific sets of frames distributed across time, with high consistency across subject cohorts and robust crossvalidation against held-out data. Optimized frame sets, despite comprising just 10% of the data, can capture stronger connectivity fingerprints than those obtained by using all data. Our findings document that individual differences in FC are distributed across both space (regions) and time (frames) and strongly suggest that FC data contain multiple spatiotemporal signatures of individual differences. We discuss our findings with special emphasis on brain–behavior relations and potential clinical applications.

Materials and methods

Approach and workflow

The main approach and workflow pursued in this study is illustrated in Fig. 1 and an overview is provided in this section. Details on each step are reported further below.

For each run of every subject, we computed the eTS as the moment-by-moment cofluctuation of the node-wise BOLD signals (Faskowitz et al. 2020). This process decomposes the time series into a matrix of all edges by time, where each frame displays cofluctuations in BOLD signal between every pair of nodes (Fig. 1A, top left). Averaging across eTS frames returns standard nodal functional connectivity (nFC) (Fig. 1A, top right). Thresholding z-scored BOLD time series yields a binary representation of the fMRI run (BOLD signal $> 0 \rightarrow 1$; BOLD signal $< 0 \rightarrow 0$) with exactly 2 cofluctuating node sets at each frame, whose agreement (AG) matrix is highly correlated with the full FC (Fig. 1A, bottom; Sporns et al. 2021). Past work on spatially localizing brain "fingerprints" (Finn et al. 2015) can be viewed as "horizontally" filtering the BOLD time courses across node sets, comprising a set of between-node edges, observed across all moments in time (Fig. 1B, top). By contrast, here, we

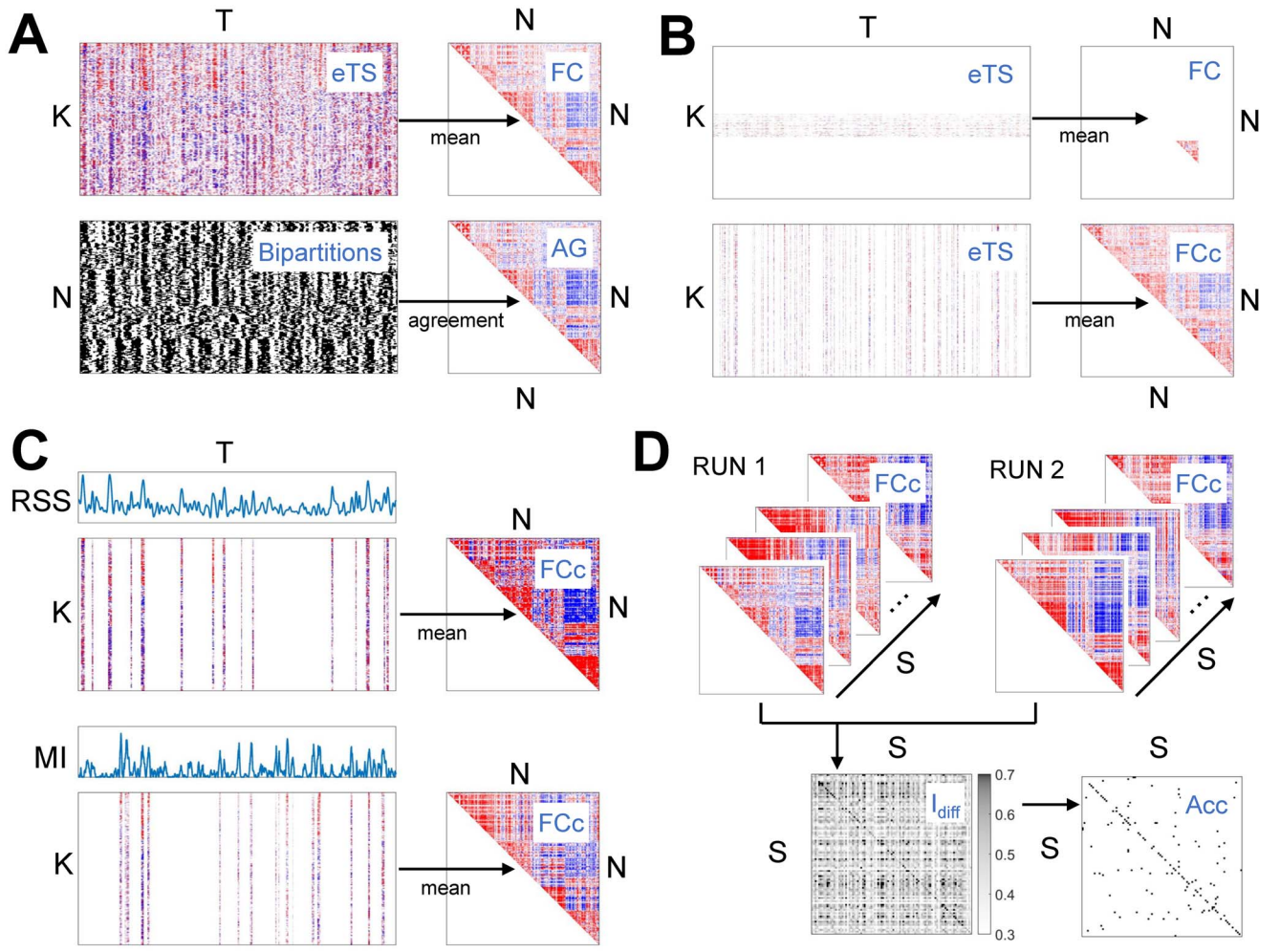

Fig. 1. Analysis and schematic workflow. A) Top: eTS forming a [$K \times T$] matrix, the mean of which, along T, is the "classic" [$N \times N$]nFC matrix. Bottom: z-scored node time series thresholded at $z = 0$ yield a [$N \times T$] matrix of bipartitions. The AG matrix of these bipartitions is very highly correlated with the nFC (Sporns et al. 2021). B) Top: Nodewise "filtering" proceeds by selecting specific nodes and their corresponding edges (rows in the eTS matrix). Computing their component nFC across all T time points may then be used for fingerprinting (Finn et al. 2015). Bottom: Framewise "filtering" proceeds by selecting moments in time (columns in the eTS matrix, corresponding to frames), which are then averaged in the T-direction to create FC components (FCc). If bipartitions are used, the frames' bipartitions are used to create AG components by computing the corresponding AG matrix. C) Selection of frames. Examples shown are RSS time series (top plots) and MI of bipartitions with a target template (bottom plots). In both cases, the top 10% of frames are selected and FC components are computed by averaging eTS at selected time points. D) FC or AG components derived from individual subjects are stacked ($N \times N \times S$; top panels) and then vectorized ($K \times S$) for individual runs. A crossrun similarity matrix is computed ($S \times S$) for each pair of runs and scored for I_{diff} or Acc (bottom panels).

filter the BOLD time courses "vertically," i.e. by selecting specific moments in time across the whole brain (all edges) (Fig. 1B, bottom). Frame selection can be random or driven by metrics that track cofluctuations within specific node sets or systems (Fig. 1C). We refer to matrices created from filtered frames as FC components, or analogously, AG components. Although not reflective of proper FC (averaged across a full set of consecutive frames), an FC component provides a matrix identical in structure which can be used to analyze temporally disparate frames highlighting a given characteristic of interest. This allows us to consider individual differences in fingerprints simultaneously both in time and across node sets as they vary their temporal expression. With this, we can systematically analyze how different features and spatiotemporal cofluctuation patterns contribute to subject identifiability.

Selection of frames can be carried out randomly, or based on a metric of interest, followed by selecting a subset of fully weighted eTS frames by the percentage desired for the given metric. Utilizing the single TR resolution of eTS, each frame can be scored based on characteristics derived directly from its cofluctuation matrix. In this study, values of the root sum square (RSS), similarity of frames within a run (SIM), velocity of transition between adjacent frames (VEL), and the mutual information with system-based templates were characterized for each frame. Framewise scores can then be binned into frame sets of any size. Here, we sectioned frames into decile bins from the highest to lowest representation of each metric and reaggregated frames within each bin into FC/AG components. We then took FC/AG components from each run of every subject and computed subject-wise similarity/distance matrices (Fig. 1D)

across pairs of runs (HCP: 6 pairwise combinations from 4 runs; MSC: 45 pairwise combinations from 10 runs). This was done for each decile bin of every framewise metric analyzed. No runs were pooled or concatenated, and pairwise comparisons of subjects on the same run were excluded. We used two of the most common distance/similarity metrics: (i) Pearson correlation and (ii) cosine distance.

Fingerprinting metrics were then computed on each frame set (FC/AG component) of these similarity matrices using 2 separate metrics referred to in the literature (Finn et al. 2015; Amico and Goñi 2018) as: (i) differential identifiability (I_{diff}) and (ii) accuracy (Acc). I_{diff} is computed by taking the difference between the average within-subject similarity versus the average between-subject similarity of FC/AG components across runs. Alternatively, Acc computes the success rate of subjects who scored highest similarity with their own FC/AG components than with other subjects. Each of these fingerprinting metrics gives us a single score for every pairwise comparison, and we averaged across the results from all combinations for each given metric bin. Summary results across all pairwise comparisons were then compared to circ-shifted nulls. These nulls were created by selecting a different subset of frames retaining the time stamps obtained in the binning step but by adding/subtracting a randomly chosen temporal offset for each given subject, run, metric, and bin. This process produced FC/AG components from time points with very similar autocorrelation and temporal spacing. However, the circ-shift operator does not simultaneously preserve any other framewise metrics, including the cofluctuation amplitudes. A total of 20 nulls were computed, per decile bin, subject, and run.

In place of preselected sets of system-based templates as the basis for frame selection, we implemented a search strategy to identify templates that, when applied to the time series, selected frames for which metrics of identifiability were optimized. Optimizations started with a randomly chosen binary template used to select the frames and then compute the identifiability. The template was modified on each iteration of the algorithm, retaining changes that resulted in increased identifiability and discarding others. The algorithm implemented simulated annealing (Metropolis et al. 1953; Kirkpatrick et al. 1983) to improve convergence onto a globally optimal solution and was run multiple times to sample different examples of optimized templates. Parameter settings related to the annealing schedule (initial temperature and cooling rate) were varied to ensure reliable convergence. To avoid overfitting, the algorithm was run on a test set of 48 subjects (comprising a random selection of half of the total sample) and was then applied to the 47 held-out subjects. Runs were carried out using different objective functions (identifiability and accuracy), using multiple random splits into training and testing data, and were carried out on both data sets (MSC data were split into sets of 5 runs each).

In summary, temporal filtering involves computing eTS, sorting frames based on framewise metrics of interest, retaining a selected subset (e.g. the top 10%) of frames, and averaging (FC component) or taking the AG matrix (AG component) of the selected frames. In this study, I_{diff} and Acc were computed for FC and AG components of all RSS, VEL, SIM, and template deciles across multiple data sets using 2 different distance/similarity metrics (Pearson correlation, cosine distance). An optimization approach was further used to guide the selection of frames that contribute the most toward identifiability and accuracy.

Participants and MRI preprocessing

The preprocessing and analysis steps were carried out on data from the Human Connectome Project (HCP; Van Essen et al. 2013). We used resting-state fMRI data from the preselected set of 100 unrelated participants (54% female, mean age = 29.11 ± 3.67, age range = 22–36), which was approved by the Washington University Institutional Review Board. Informed consent was obtained from all participants, and they were instructed to keep their eyes fixated on a cross when in the scanner. Each participant completed 4 15-min resting-state fMRI runs over a period of 2 days, where 2 runs were collected on each separate day. fMRI data were obtained using a gradient-echo EPI sequence, resulting in a run duration of 14:33 min per run (TR = 720 ms, echo time (TE) = 33.1, flip angle = 52, 2-mm isotropic voxel resolution, multiband factor = 8). A 3T Siemens Connectome Skyra with a 32-channel head coil was used for data collection. Refer to Glasser et al. (2013) for full details about the data acquisition and the minimal preprocessing pipeline. Four subjects were excluded based on outlier motion summary statistics (see Sporns et al. (2021), and 1 subject was excluded due to software error from diffusion magnetic resonance imaging (dMRI) processing). The 95 included subjects had the following demographic characteristics: 56% female, mean age = 29.29 ± 3.66, age range = 22–36. The data had been previously preprocessed for another study and thorough details can be found in Sporns et al. (2021) and Esfahlani et al. (2022).

Data from the Midnight Scan Club (MSC) was used as a confirmation analysis and had also been collected with parameters detailed in Gordon et al. (2017) and is publicly available at https://openneuro.org/datasets/ds000224/versions/00002. Data included 10 healthy, young adult participants (50% females; age range = 24–34) who were recruited at Washington University. Informed consent was obtained from each participant and the study was approved by the Washington University School of Medicine Human Studies Committee and Institutional Review Board. A Siemens TRIO 3T MRI scanner was used over 12 separate runs at midnight and collected over multiple days. Ultimately, 5 h of resting-state fMRI data were collected for each participant. The data were run through fMRIPrep (version 20.2.0) to obtain minimally

preprocessed functional data in the fs_LR surface space. Please refer to Esteban et al. (2019) for a description of the processing pipeline and to https://fmriprep.org/en/20.2.0/citing.html for a complete description of this version of the image processing pipeline. The pipeline was run using the following options: FreeSurfer (version 6.0.1); "fieldmap-less" susceptibility distortion correction; the NKI skull stripping template; slice-time correction; 6° of freedom for the BOLD-T1w coregistration.

All functional data were linearly detrended, band-pass filtered (0.008–0.08 Hz) (Parkes et al. 2018), confound-regressed, and standardized using Nilearn signal.clean. Functional data of the HCP data set were already provided in a form that was cleaned of signal artifacts using the ICA FIX methodology (Salimi-Khorshidi et al. 2014). These functional data were further nuisance-regressed using the global signal, the derivative of this signal, and the squares of these previous 2 terms. Functional data of the MSC data were nuisance regressed using 6 motion estimates, time series of the mean cerebrospinal fluid, mean white matter and global signal, the derivatives of these 9 regressors, and the squares of these previous 18 terms (Satterthwaite et al. 2013).

For obtaining regional time series, we employed the Schaefer 200 functional parcellation (Schaefer et al. 2018), a parcellation constructed to optimize the local gradient and global similarity of the fMRI signal within nodal areas. For both data sets, the Schaefer 200 parcellation was provided in the fs_LR surface space. Nuisance-regressed functional data were averaged within each node at each frame, forming 200 spatially distinct time series. We mapped the 200 nodes to a set of canonical functional networks determined by Yeo et al. (2011). Specifically, we used seven canonical functional systems: visual (VIS), somatomotor (SOM), dorsal attention (DAN), ventral attention (VAN), limbic (LIM), frontoparietal (FP), and default mode (DMN).

FC and eTS

FC in fMRI measures the statistical dependencies between the BOLD time series of every pair of brain regions. One definition of the Pearson correlation is that it is the mean of the moment-by-moment product of the normalized (z-scored) time series, calculated as

$$r_{ij} = \frac{1}{T-1}\sum_{t=1}^{T} z_i(t) * z_j(t), \quad (1)$$

where there are T samples for each moment in time (t) and the z-score for a region x is represented as $z_x = [z_x(1), \ldots, z_x(T)]$. This results in a linear similarity that can be either positive or negative. When computed for each pair of regions, this produces an $[N \times N]$ matrix, where N is the number of nodes (brain regions). Due to the symmetry of the correlation matrix, the upper triangular portion of the matrix is vectorized into all unique entries, $K = (N^2 - N)/2$, and used in the following FC analyses.

eTS decomposes FC into a $[K \times T]$ matrix of all edges (K) by time (T), where each frame at time t displays cofluctuations in BOLD signal between every pair of nodes computed as $z_i(t) * z_j(t)$ (cf. Fig. 1A, top); (Faskowitz et al. 2020). The measure can be best thought of as the Pearson correlation excluding the final averaging step. A single entry in the matrix of eTS represents the instantaneous product between the respective time series of a given node pair, i.e. each edge corresponds to a single node pair. Cofluctuation is positive when the signs of the 2 activity values agree (both positive, or both negative) and negative otherwise. Averaging cofluctuations across time for all edges returns standard nFC.

Bipartitions and AG matrices

The eTS can be binarized by removing amplitude and retaining the sign, resulting, at each temporal frame, in a series of bipartitions (Sporns et al. 2021). Each bipartition consists of exactly 2 sets of nodes that divide the network into 2 opposing communities of regions that positively cofluctuate within their own community but negatively cofluctuate across communities. Binarized eTS frames can be converted into an $[N \times N]$ matrix by computing an AG matrix across all or a subset of frames. This AG matrix, also called coclassification matrix (Jeub et al. 2018), expresses the frequency with which each node pair is assigned to the same community. Each binarized eTS frame constitutes a bipartition. For each such bipartition we record, for each of the $[N \times N]$ node pairs, whether the 2 nodes are in the same community. The mean (over all T partitions) of such "agreements" in community membership constitutes the AG matrix. These values are compared to a null by subtracting the expected frequency of nodes identifying with the same community after group labels have been randomly permuted (Jeub et al. 2018). Thus, a node pair that maintains the same cofluctuation patterns across most frames (exceeding the null) will result in a positive entry in the AG matrix, while a node pair that often differs in community labels (with less AG than expected by chance) will produce a negative entry. Despite removing all signal amplitudes and retaining only the signs of interaction terms, the resulting AG matrix is very highly correlated with standard nFC when computed across the full eTS (Sporns et al. 2021).

Framewise metrics

All eTS frames for each subject and every run were assigned values for each of the following framewise metrics.

Cofluctuation amplitude (RSS), similarity (SIM), velocity (VEL), framewise displacement (FD)

The RSS can be used to measure the overall amplitude of cofluctuations across all node pairs for each eTS frame. This metric summarizes the deviation from 0 of all edge (node pair) cofluctuations. High RSS would signify that the cofluctuations of most node pairs in that frame display high positive or negative cofluctuations. A low

RSS value would imply that most node pairs exhibit smaller cofluctuations. The square of each cofluctuation is calculated and summed across all edges within an eTS frame, and a single RSS value is assigned to each moment in time.

Similarity (SIM) was computed as the average mutual information, computed on bipartitions, between a given frame and every other frame in the run. This operation results in a mean SIM value for each moment in time, i.e. a vector of length T. Mutual information is computed as described previously (Rubinov and Sporns 2010; Sporns et al. 2021).

Velocity (VEL) was computed as the similarity (cosine distance) between the cofluctuation matrices of a given frame and the frame preceding it in time. This operation results in a vector of values of length $T-1$, for each single run of length T.

Framewise displacement (FD) was derived from the preprocessing of the HCP and MSC data, resulting in a single value for each frame of each run, i.e. a vector of length T.

System-based templates

In binarized eTS, each moment in time can be defined as bipartitioning the network into 2 complementary communities. How nodes divide into these communities can further be analyzed according to how well each empirical bipartition matches a set of template patterns that split the network along combinations of functional systems (Sporns et al. 2021). These template patterns account for every combination of bipartitioning the network within and between groups of 7 functional systems (Yeo et al. 2011). Given the canonical set of 7 systems, there are 7 templates that divide the set into 1 versus 6 systems, 21 templates that divide them into 2 versus 5 systems, and 35 templates that divide them into 3 versus 4 systems for a total of 63 such templates. Mutual information was computed for each frame with the full template set, creating 63 mutual information time series for every run and subject. Frame filtering was then used, as outlined above, to isolate the top 10% of frames that best match each template pattern.

Frame-shifted null

Each filtered decile bin was compared to an equal subset of frames selected with random relation to the metric of interest. This was done by shifting the index of all frames for the given metric either to the right or left by a random offset (chosen uniformly between a minimum of 10 frames and a maximum of 1,090 frames for HCP or 790 frames for MSC using Matlab's circ-shift operator) and selecting those offset frames for analysis. Frame selection that extended beyond the bounds of the time series were circularly shifted to the opposite end of the time series. This largely maintained the general temporal spacing and autocorrelation of the frames while randomizing relation to the metric of interest. A set of 20 independent "circ-shift" nulls were created for each decile, metric, and subject. To assess the magnitude of autocorrelation in HCP and SC data, we calculated the Pearson correlation between eTS frames, using lags of −50 to +50 frames, over all subjects and all runs.

Cross-subject similarity/distance

FC and AG components that were created from all or filtered eTS frames formed stacks of $[N \times N]$ matrices, the upper triangles of which were converted into vectors of size $(N^2 - N)/2$. The similarity or distance between subjects was computed between vectorized FC/AG components of all S subjects across two separate runs (cf. Fig. 1D). This creates an $[S \times S]$ matrix of the relation between all pairs of subjects for a given pair of runs. Similarity between components is assessed using 2 metrics, the Pearson correlation, and the cosine distance.

Fingerprinting metrics

Identifiability was computed utilizing 2 measures that assess whether an individual is more similar with themselves or with others across a pair of runs. These analyses were done on the resulting similarity/distance matrices described above, where the diagonal of each matrix represents the subject's similarity with themselves across runs and all off-diagonal values are combinations of different subjects across the 2 runs. In Amico and Goñi (2018), differential identifiability (I_{diff}) was computed as

$$I_{\text{diff}} = (I_{\text{self}} - I_{\text{others}})^* 100, \quad (2)$$

where I_{self} refers to the mean of the diagonal elements of the $[S \times S]$ distance/similarity matrix and I_{others} is the mean of the off-diagonal elements.

Accuracy (Acc) is computed as the frequency of all subjects (95 total) that successfully identified with themselves across runs. This is done by determining whether the value of the main diagonal (self-similarity) is the maximum value across the rows and columns of the matrix. Since the similarity/distance matrices are asymmetric, this can be done separately across both columns and rows of the matrix. In this work, to allow for a single measure of success rate, we first symmetrized the similarity/distance matrices and then computed a single value for accuracy. Acc is a stricter metric than I_{diff} as it is all-or-none compared to the continuous similarity/distance scale used to compute I_{diff}. Since Acc is bounded between 0 and 1, it can be directly interpreted as the percentage of instances that subjects identified more strongly with themselves than with all others, evaluated across all pairwise comparisons.

Optimization

In addition to using preconfigured templates to select framesets for computing identifiability, we implemented an optimization algorithm to automatically search for templates that would yield framesets for which identifiability metrics are maximized. The algorithm was carried out on the AG components for reasons of computational

expediency. Basically, starting from a randomly configured template, the algorithm will apply the template to all training data, select best matching frames, retrieve them to create AG components for all subjects and all runs, and then compute identifiability or accuracy. Then, in a new iteration of the algorithm, the template is modified, and the identifiability or accuracy achieved with the modified template is compared to the previous iteration. If the metric improves, the modified template is retained. Optimizations are run for 25,000 iterations to ensure that a stable end state has been reached.

The possible space of templates (binary, composed of N nodes) is large (2^N) and cannot be probed exhaustively. To search the space efficiently, we used an implementation of the Metropolis-Hastings algorithm (Metropolis et al. 1953). At each iteration of the algorithm, the current values of the objective function D (identifiability or accuracy) are either accepted or rejected, with rejection or acceptance governed by simulated annealing (Kirkpatrick et al. 1983). New variants are accepted if the objective function improves (better identifiability or accuracy) or if the annealing criterion $e^{-\Delta D/\mathbf{Temp}} > R(0,1)$ is fulfilled, where **Temp** refers to a simulated "temperature" and $R(0,1)$ is a random number uniformly drawn from the $[0,1]$ interval. Essentially, the annealing criterion allows suboptimal variants to pass as a function of the current temperature. At high temperatures, the algorithm will tend to reject local optima in favor of continued exploration, while at low temperatures, exploration is limited to the immediate vicinity of the current best solution. The temperature decays as $\mathbf{Temp} = T_0 T_{\mathbf{exp}}{}^h$, with parameters T_0 and $T_{\mathbf{exp}}$ selected to ensure convergence in a reasonable time. The initial condition was a completely random template, with each node belonging to 1 of 2 communities with equal probability. On each step of the optimization, ≥1 nodes were flipped, with the number of flips determined by a normal distribution (frequencies of 1, 2, and 3 element flips were 0.68, 0.27, and 0.04, respectively). Two different objective functions were tested, identifiability and accuracy, both computed based on the $[S \times S]$ Pearson correlation of the AG components.

Optimizations were run 24 times to sample different examples of optimized templates. These templates were then compared to each other as well as to the 63 canonical template set. The framesets selected by these templates were examined for their cofluctuation amplitude and for the consistency, across multiple optimization experiments, with which specific time points were selected.

To determine if templates with optimal identifiability or accuracy could be successfully applied to held-out data, we ran optimizations on a training set of subjects (randomly chosen to comprise 48 out of the 95 total set) and then optimized templates were tested on the remaining subject set.

To check consistency with prior work carried out in node space (Finn et al. 2015; Peña-Gómez et al. 2018), optimizations were also conducted by selecting node sets instead of framesets. This resulted in full FC estimates for each node set, across all subjects and runs, which were then used to compute identifiability and accuracy metrics. Optimizations were implemented as described above using a simulated annealing algorithm on nFC pattern for specific (optimized) node sets. Initially, a random node set of size "ns" (out of $n = 200$) was selected, and in subsequent iterations, nodes were swapped to optimize the objective function. The final set of "ns" nodes was retained for further analysis, and 96 optimizations were carried out in total to determine robust convergence. Results are reported for ns = 40.

Results

Individual differences in full runs and in random subsets of frames

Baseline values of differential identifiability (I_{diff}) and accuracy (Acc) are shown for the full run and across random frame subsets of increasing size (Fig. 2). Random frame sets were chosen to establish how fingerprinting metrics vary as sample sizes increase. It is known that FC estimates improve with longer runs (Laumann et al. 2015), so the quality of fingerprinting is expected to vary based on number of frames alone. We selected random sets of frames, with sets increasing in size from 55 to 1,045 frames in increments of 55. Each of these random sample sizes (19 total) were turned into FC/AG components and their identifiability scores were compared against full nFC. Results from size-matched random frames were used as a baseline for all filtered decile analyses (see below). Random selections were performed for 20 times for each of the 19 settings.

In general, both fingerprinting metrics improve as frame sets increase in size up to around selecting half of the entire run. This trend is observed regardless of binarization (FC or AG), data set (HCP or MSC), and similarity/distance metric (Pearson or cosine) (Fig. 2, Supplementary Fig. S1). Although findings were largely consistent across data sets, the MSC metrics were higher than HCP across all measures. This resulted in the Acc baseline for MSC achieving near-maximum values for even the smaller frame bins, with a slight decrease in the smallest subset (5% frames). This is possibly due to the smaller size or composition of the cohort, the length of resting-state runs, or differences in the preprocessing pipeline. Subsequent analyses were compared to baseline values specific to each measure.

Individual differences vary with cofluctuation amplitude

A conspicuous feature of eTS is the occurrence of intermittent, short-lasting bursts of high cofluctuation (Esfahlani et al. 2020) computed as the RSS amplitude of the system-wide cofluctuations. These "events" have recognizable, somewhat stereotypic topography, and involve specific systems and brain-wide patterns (Esfahlani et al. 2020; Jo et al. 2021a; Sporns et al. 2021; Betzel et al. 2022).

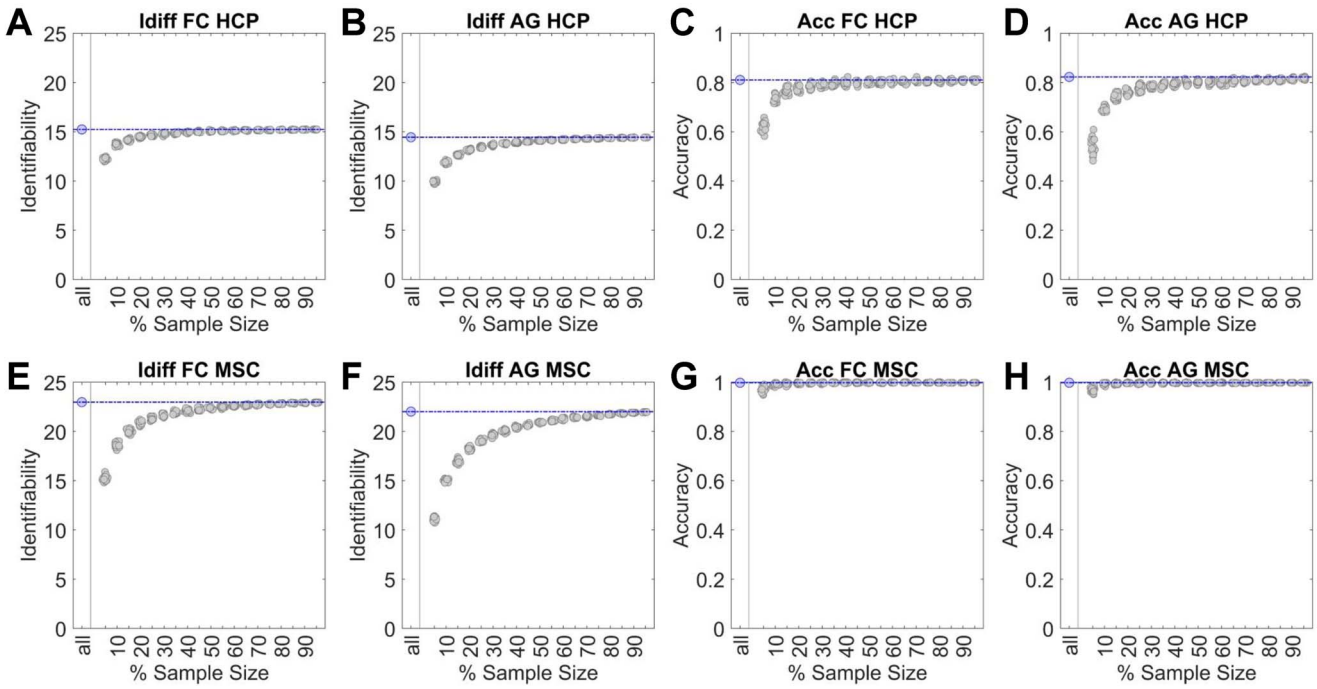

Fig. 2. Fingerprinting metrics in full data and in random samples of increasing size. Each panel displays average identifiability (I_{diff}; panels A, B, E, F) or accuracy (Acc; panels C, D, G, H) for random frame samples of varying percentages of the full run (in 5% steps or 55 frames). For each setting of sample size, 20 random samples were taken (plotted in gray). Metrics are compared to those obtained from full data sets, either full FC or full AG (blue lines). The panels show results for all combinations of either identifiability (I_{diff}) or accuracy (Acc), FC or AG components, and data sets (HCP or MSC).

Here, we examine whether the magnitude and spatial patterns of individual differences, computed from subsets of fMRI frames, vary systematically with RSS amplitude. Examples of individual and group RSS decile components are shown in (Supplementary Figs. S2 and S3).

We found a marked decrease in identifiability with lower RSS amplitudes in both data sets (Fig. 3). Similar trends were found when cosine was used in place of Pearson correlation to create the cross-subject similarity matrix (Supplementary Fig. S4). The first 3 RSS decile bins outperform the corresponding frame-shifted nulls and achieve significantly higher results than the lowest RSS decile bins for both the FC and AG components. For the HCP data, none of the bins outperform the full FC/AG nor randomly selected frames. The first few bins of the MSC data, however, do outperform randomly selected frames. For accuracy, RSS decile bins show a nonlinear relationship in which accuracy peaks for the mid RSS deciles, exceeding both the frame-shifted nulls and the random frames (Fig. 3). Interestingly, this increase in accuracy for midamplitude frames above the nulls largely disappears in the AG components, implying that improvements in accuracy may be largely based on reliable variations in BOLD amplitude rather than the binarized pattern where amplitude is discarded. Results in MSC reach near 100% accuracy and show a decrease in accuracy within the highest RSS decile. Once again, these trends are also found using cosine distance (Supplementary Fig. S4).

Confirming and extending earlier results (Esfahlani et al. 2020; Betzel et al. 2022), these findings show that frames selected based on RSS amplitude show varying levels of identifiability and accuracy. Further extending the analysis, we examined the effect of RSS on both the identifiability and accuracy by progressively removing the RSS deciles in order of highest to lowest amplitude (retaining 90% of the data, then 80%, then 70%, and so forth). Results shown in Fig. 4 indicate that by removing the highest RSS amplitude frames (containing most of the significant RSS-amplitude peaks labeled "events"), identifiability drops below null values while accuracy improves. Indeed, while identifiability continues to drop as more data are removed, accuracy reaches highest levels (above the null permutations) and outperforms the level attained with the full data set when the top 40% RSS-amplitude frames are removed. This implies that higher amplitude frames promote higher identifiability while accuracy increases even above the levels afforded by full FC upon removal of the higher-amplitude RSS frames.

In summary, identifiability and accuracy distribute differently across RSS values, with identifiability highest in top-RSS frames and accuracy highest in mid-RSS frames. Removing higher-amplitude RSS frames diminishes identifiability but boosts accuracy.

Individual differences vary with framewise metrics

High-amplitude frames have been shown to exhibit somewhat consistent topography (spatial pattern; Esfahlani et al. 2020), are more stereotypic than low-amplitude frames (Esfahlani et al. 2020; Sporns et al. 2021; Betzel et al. 2022), and represent moments in time

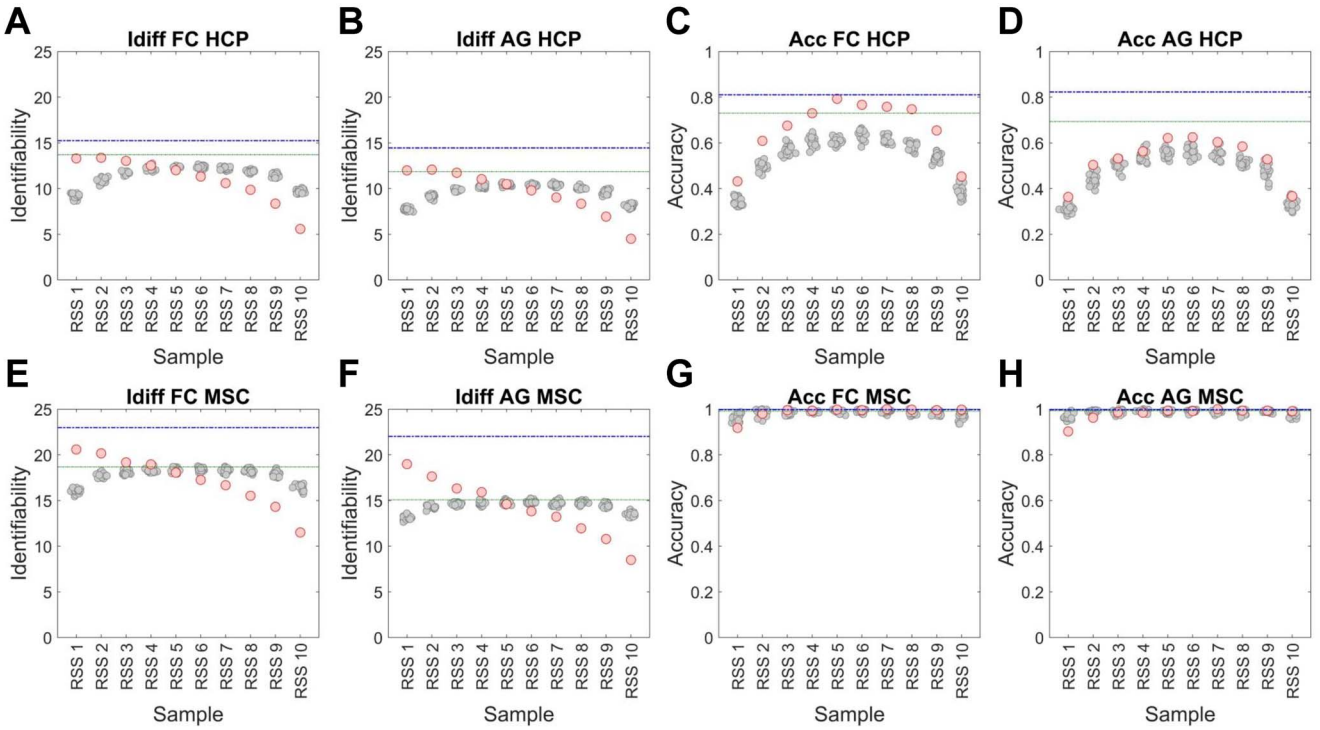

Fig. 3. Variation of fingerprinting metrics with cofluctuation amplitude (RSS). Each panel displays average identifiability (I_{diff}; panels A, B, E, F) or accuracy (Acc; panels C, D, G, H) across subjects for each decile of frames from highest (RSS1) to lowest (RSS10) amplitude (red dots). The identifiability or accuracy for 20 randomly circ-shifted nulls (gray dots) were computed separately for each decile. Size-matched random deciles (corresponding to random samples of 10% of the frames) derived from baseline analyses (Fig. 2; green line) and full data sets (blue line) are shown for comparison. The panels show results for all combinations of either identifiability (I_{diff}) or accuracy (Acc), FC or AG components, and data sets (HCP or MSC).

when the spatial cofluctuation patterns are temporally more stable (Sporns et al. 2021). To examine how fingerprinting metrics vary in relation to these temporal characteristics, we computed 2 additional framewise metrics: similarity (SIM; computed as the mean mutual information between each frame with all other frames in the run) and velocity (VEL; rate-of-change between frames computed as the cosine similarity between temporally adjacent frames). Both are related to RSS, with RSS and SIM showing a strong positive relationship ($\hat{\rho} = 0.555$; mean Spearman's ρ, all subjects, all runs, HCP), RSS and VEL showing a strong nonlinear negative relationship ($\hat{\rho} = -0.693$), and SIM and VEL showing a strong negative relationship ($\hat{\rho} = -0.469$). Therefore, high cofluctuation amplitudes largely occur during frames that have the highest similarity across the run and have the lowest velocity of frame transitions. These relations likely follow from high RSS frames strongly deviating from mean brain activity and therefore being slower to transition toward and away from high RSS activity patterns. This would cause adjacent frames to become more similar and the rate of change to decrease with increasing RSS. As expected, frames filtered based on cofluctuation amplitude and similarity within a run appear to yield comparable identifiability, while velocity has a largely inverse relationship with both metrics. High SIM frames outperform both nulls and random frames for identifiability, while mid-SIM deciles show the highest accuracy (Fig. 5). Lower VEL deciles display the highest identifiability, while accuracy peaks for the second and third deciles at levels above full FC.

To account for possible effects of involuntary head motion during scanning, we first examined whether there is a systematic relationship between FD and cofluctuation amplitude (RSS). As shown in prior work, RSS and FD are uncorrelated and selecting subsets of frames, for example, by binning RSS into deciles, does not result in systematic variation of FD across bins (Supplementary Fig. S5). Second, we treated FD as a framewise metric used for filtering and binning frames. Apart from the set of frames with the highest motion, which shows a small negative deflection in both I_{diff} and Acc, no systematic variation in fingerprinting metrics is observed (Supplementary Fig. S6). Indeed, FD binning results in values for I_{diff} and Acc which are very close to those obtained for random samples of the same size and overlap with frame-shifted nulls. Taken together, these analyses suggest that FD has negligible impact on fingerprinting metrics.

These results reveal that maximal identifiability and accuracy display different frame characteristics, where higher RSS, SIM, and lower VEL frames favor high identifiability, while accuracy largely selects against extremes associated with these framewise features.

Individual differences vary with temporal expression of functional systems

A seminal finding in previous "fingerprinting" studies showed that different functional systems, for example,

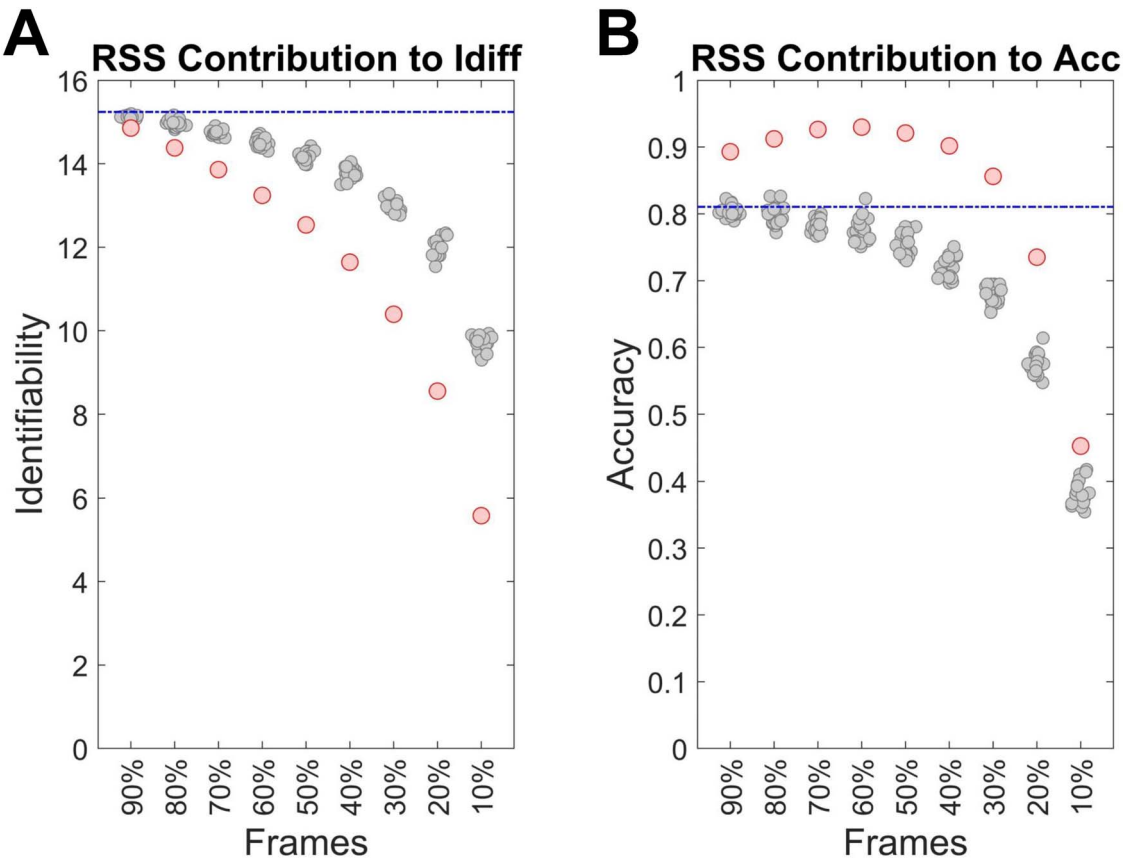

Fig. 4. Variation of fingerprinting metrics after removal of high-amplitude frames. A) Average identifiability (I_{diff}) and B) accuracy (Acc) are shown (red dots). Bins progressively remove RSS bins (deciles), starting with the top decile (90% of frames retained), then removing the 2 top bins (80% of frames retained), and so forth. Accordingly, frame sets decrease in size from left to right, starting with 90% of frames in sample 1 and decreasing by 10% each consecutive sample until only 10% frames remain. Results in each bin were compared to 20 circ-shifted nulls (gray dots) and full FC (blue line). The analysis is carried out in the HCP data set.

canonical resting-state networks (RSNs), such as those originally reported by Power et al. (2011) and Yeo et al. (2011), differentially contribute to individual differences (Mira-Dominguez et al. 2014; Finn et al. 2015; Airan et al. 2016; Amico and Goñi 2018; Gratton et al. 2018; Peña-Gómez et al. 2018; Ravindra et al. 2021; Sareen et al. 2021). We confirmed this finding in our data, with high identifiability and high accuracy (above all 100 null permutations performed) found in the FP system (Supplementary Fig. S7).

Prior work demonstrated that the expression of canonical functional systems varies across time and can be described with a template basis set using 63 combinations of the 7 Yeo systems, where each template encompasses bipartitions between systems (Yeo et al. 2011; Sporns et al. 2021; Fig. 6A and B). In Sporns et al. (2021), we found that variations in system expression result in fluctuations in fingerprinting metrics across time. Here, we expand on these analyses by systematically comparing template-based identifiability and accuracy across the HCP and MSC data sets to determine if specific templates can consistently isolate more identifiable frames. As shown in Fig. 6C, we find a positive relationship between HCP template identifiability and accuracy (HCP: $= 0.589, P = 3.7{*}10^{-7}$; MSC: $\rho = 0.614, P = 8.7{*}10^{-8}$) and show that 14 templates have both higher identifiability and accuracy compared to the null models (across at least 5 of the 6 pairwise comparisons). Among the best-performing templates, with a template-specific I_{diff} that exceeds that for the full FC data, is template 24, which corresponds to cofluctuations within the VAN plus FP systems, relative to the rest of the brain (Fig. 6B, middle). The prominence of these 2 functional systems is consistent with previous literature on "fingerprinting" across full node time series (Mira-Dominguez et al. 2014; Finn et al. 2015; Airan et al. 2016; Amico and Goñi 2018; Gratton et al. 2018; Peña-Gómez et al. 2018; Ravindra et al. 2021; Sareen et al. 2021). Both template-specific fingerprinting metrics are significantly correlated across both data sets (I_{diff} : $\rho = 0.401, P = 0.001$; Acc : $\rho = 0.56, P = 3.6{*}10^{-6}$), suggesting that template rankings are preserved. Taken together, our findings suggest that previously reported findings based on spatial filtering (node or system selection while using full FC runs) may largely be driven by moments in time where those nodes and systems exhibit high cofluctuations.

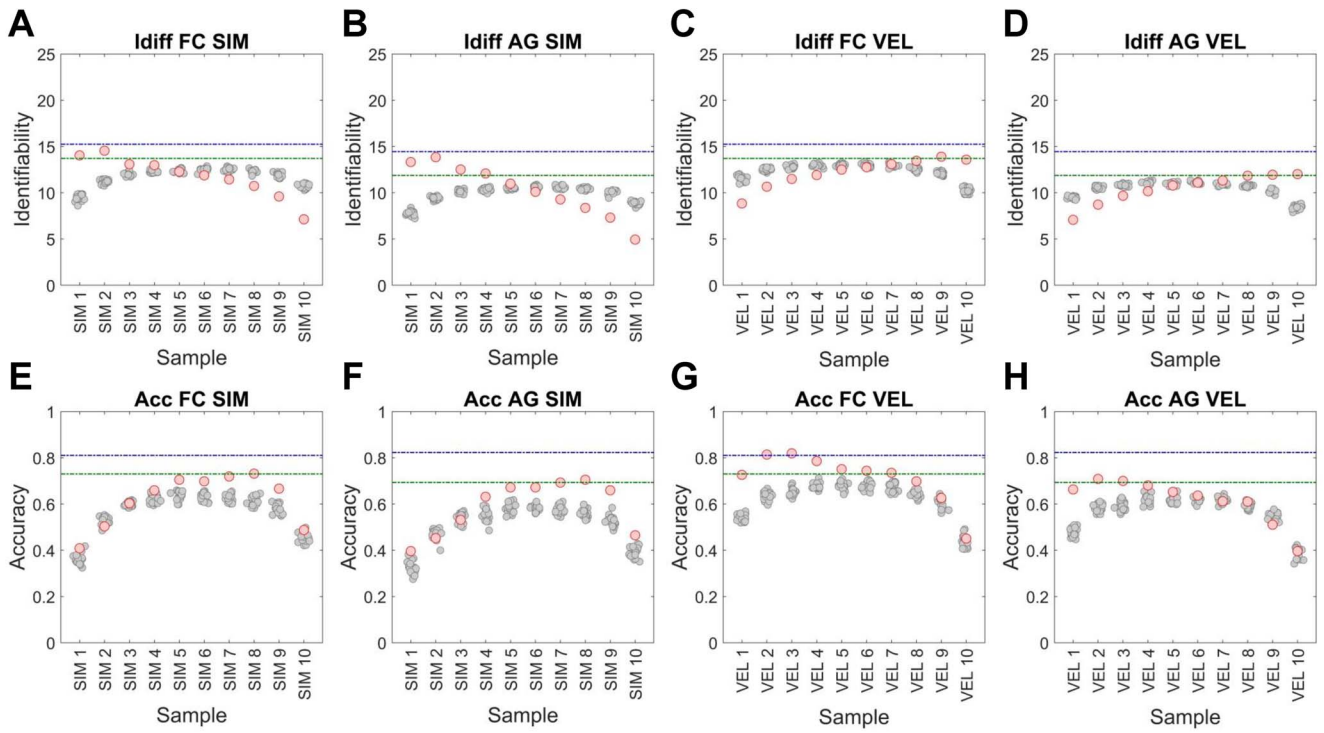

Fig. 5. Variation of fingerprinting metrics with SIM and VEL deciles. Each panel displays average identifiability (I_{diff}; panels A–D) or accuracy (Acc; panels E–H) across subjects for each decile of frames from highest to lowest similarity (SIM; panels A, B, E, F) or velocity (VEL; panels C, D, G, H), with all data points indicated by red dots. SIM was computed for each frame as the mean mutual information between that frame and all other frames in the run. VEL was computed for each frame as the cosine similarity between that frame and the preceding frame. Frame sets were selected by binning frames into deciles for each metric. The average identifiability or accuracy for 20 circ-shifted nulls (gray dots) were computed separately for each decile. Size-matched (10%) random samples from baseline analyses (Fig. 2; green line) and full data sets (blue line) are shown for comparison. The panels show results for all combinations of either identifiability (I_{diff}) or accuracy (Acc), FC or AG components, and metric (SIM or VEL). All data are from the HCP sample.

Optimization of individual differences

The previous analyses have identified some key factors that yield strong individual differences in space (node sets specific to functional systems; Finn et al. 2015) and in time (subsets of frames selected according to different temporal criteria; Amico and Goñi 2018). In this final section, we deploy identifiability and accuracy as objective functions in a data-driven search algorithm to identify node sets (see also Peña-Gómez et al. 2018) and moments in time that yield optimal "fingerprinting."

Figure 7 shows findings from optimizations that search node space. Optimizing I_{diff} yields 2 distinct sets of solutions. Highest I_{diff} is found with a fingerprint that centers mainly on the VAN system, entirely excluding participation of FP nodes (pattern "P1"; Fig. 7A). A second, somewhat less optimal fingerprint, is centered on the FP system with participation from other systems, including LIM, DMN, and VAN (pattern "P2"; Fig. 7A). Optimizing Acc, in turn, yields a single family of solutions (Fig. 7B) whose average regional and systems profile centers on FP, DMN, LIM, and VAN, strongly resembling pattern "P2" found when optimizing I_{diff}. Results are robust across different sizes of node sets, with results for 40 nodes, as shown in Fig. 7. Comparable, though smaller, patterns are seen for sets of 30, 20, and 10 nodes (data not shown).

Figure 8 shows findings from optimizations that search over frames (time) by varying a binary template used to compute and rank mutual information with bipartitions of individual frames. This approach allows selecting frames based on a "temporal filter" that can be uniformly applied to all subjects and all runs. We use I_{diff} and Acc as objective functions (Fig. 8A and B, respectively), retrieve the selected (binary) templates and compare them across different runs of the algorithm (Fig. 8A and B; left panels), and show mean AG patterns for the selected AG components as well as for the selected components minus the initial components (Fig. 8A and B; middle panels). Results indicate that the optimization algorithm successfully identifies templates that generate greatly increased I_{diff} or Acc compared to the initial condition. Multiple runs optimizing I_{diff} (Fig. 8A) converge onto a set of templates that are somewhat consistent in the pattern of bipartition they describe. When computing the NMI between each selected bipartition (24 runs) with each canonical system template (63) and comparing initial (random) bipartitions to selected (optimized) bipartitions, optimized templates exhibit significant ($P < 0.05/63$, Bonferroni-corrected) NMI with 22 canonical templates. By contrast, multiple runs optimizing Acc (Fig. 8B) yield a heterogeneous set of patterns, each of which satisfies the optimization

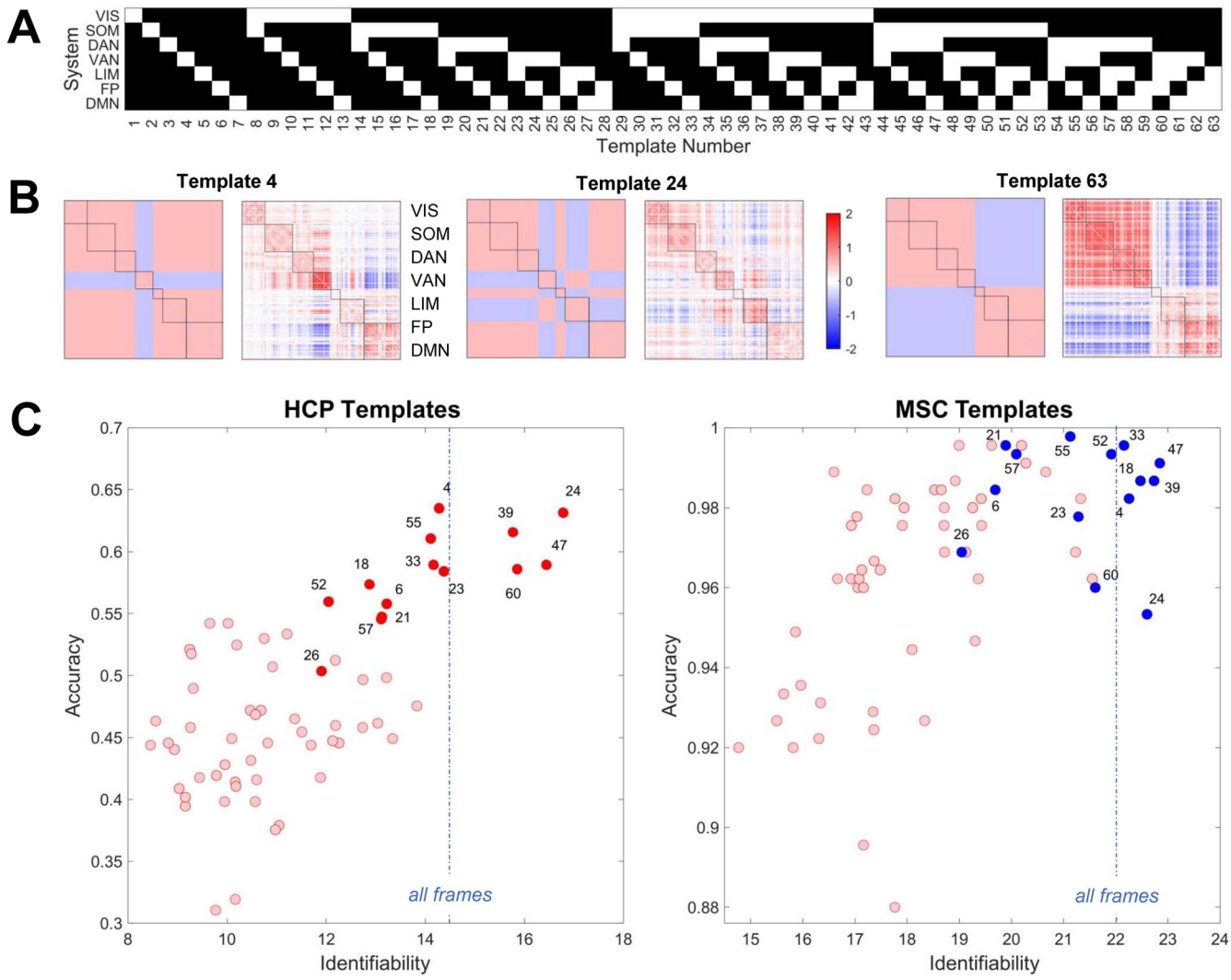

Fig. 6. Template-based filtering and effect on identifiability and accuracy. A) Template basis set comprising 63 templates that divide the 200 nodes of the original network into 2 node sets (a bipartition) along the borders of 7 canonical functional systems (Sporns et al. 2021). For example, template 43 defines a bipartition of the brain into 1 node set comprising VIS, FP, and DMN (labeled white) and a second complementary node set comprising SOM, DAN, VAN, and LIM (labeled black). In the bipartition framework, the 2 node sets represent 2 cofluctuating communities, with the union of these 2 communities covering the entire 200 node network. B) Mean FC components (all subjects, all runs, HCP data) created from filtering for template 4 (VAN against the rest), template 24 (VAN and FP against the rest), and template 63 (LIM, FP, and DMN against the rest). C) Mean identifiability and accuracy were computed for each template across all subjects and runs for both the HCP data set (left) and the MSC data set (right). Circ-shifted nulls were generated for each template and only templates that exceeded all nulls in 5 out of 6 pairwise runs were labeled for the HCP data (left; dark red). The same templates are highlighted in blue in the MSC data (right panel) to show correspondence in rankings across data sets. Performance level for I_{diff} when using all frames (full runs) is indicated by a blue line.

criterion but through different patterns of bipartitions. No significant consistency in NMI between optimized templates and canonical templates is found. These differences in consistency between templates when optimizing I_{diff} versus Acc are reflected in differences in frame attributes (Fig. 8A and B; right panels). Optimizing I_{diff} results in more consistent selection of time points across runs and in framesets that are enriched in high cofluctuation amplitude (RSS). By contrast, optimizing Acc results in time points that are highly variable between runs, with greater participation of mid- to low-RSS frames.

Results in Fig. 8 are for optimizations carried out on HCP data (48 training-set subjects, all runs). We tested the robustness of our findings in the following ways. In HCP data, we applied optimized templates to held-out subjects, testing a total of four random splits into 48 training and 47 testing subjects (both sets using all four runs). We carried out optimizations for I_{diff} on the training set and then applied the optimized templates to the held-out testing set. Improved fingerprinting performance carries over between training and testing set for both I_{diff} and Acc and for all 4 splits (Supplementary Fig. S8). The same outcome is obtained when training and testing set are split by runs (HCP data; training: all subjects, runs 1 and 2, 1 and 3, 2 and 4, 3 and 4, respectively; testing: all subjects, runs 3 and 4, 2 and 4, 1 and 3, 1 and 2, respectively; Supplementary Fig. S9). Finally, consistent findings are obtained when optimizations are run on MSC data (all subjects, 5 runs

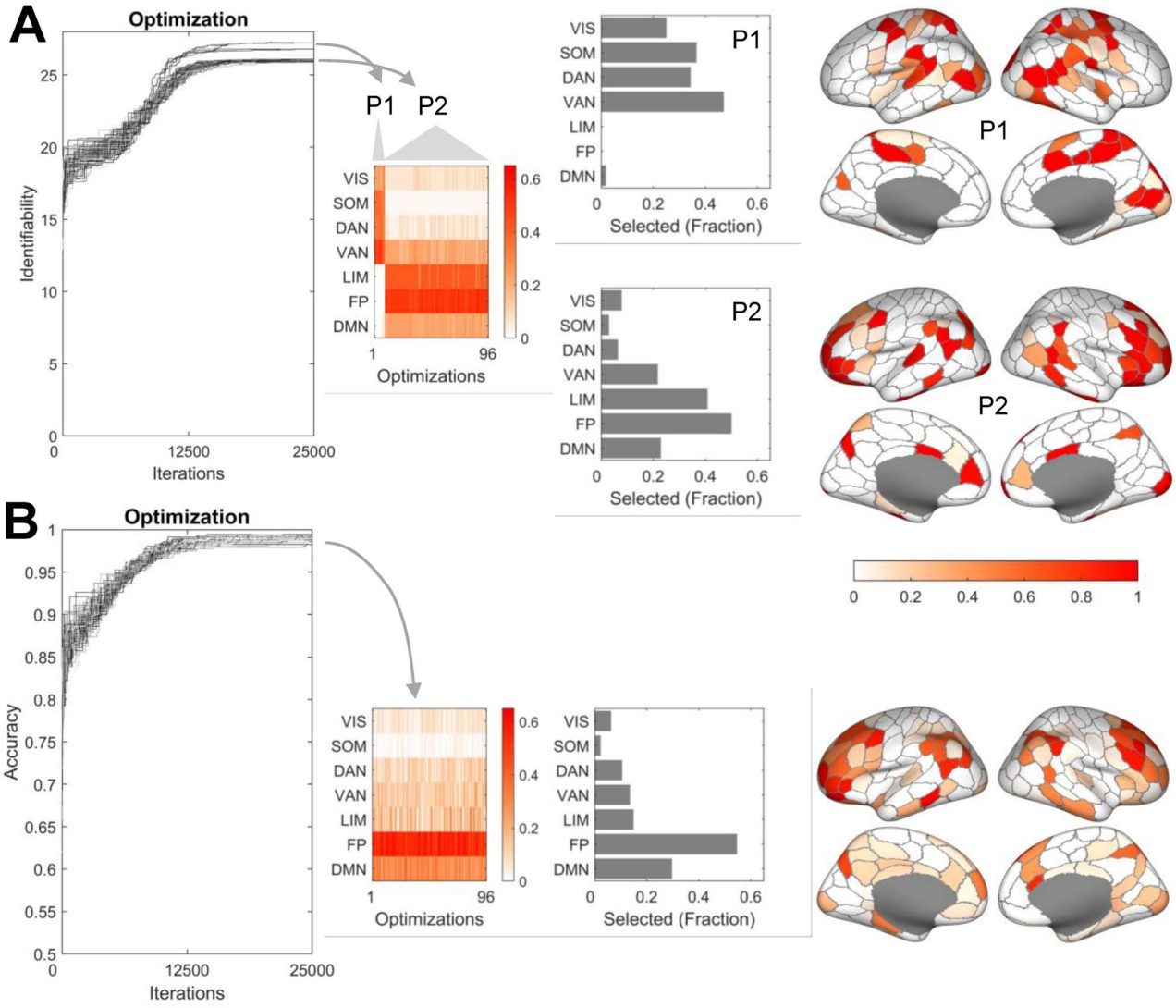

Fig. 7. Node set optimizations. A) Plot at left shows the evolution of the objective function for 96 runs of the optimization, with I_{diff} as the objective and with 40 nodes (out of 200) in the optimized set. Note different levels of convergence, indicating qualitatively different levels of performance. "P1" and "P2" refer to the two main patterns of convergence (9 examples for P1, 87 examples for P2; P1 comprises 5 and P2 comprises 27 unique outcomes). Plots in the middle indicate contributions of canonical functional systems (expressed as the mean contribution of each functional system to the optimized 40-node set). Plots at the right show cortical maps of the contributing regions for patterns "P1" (top) and "P2" (bottom), respectively. Color scale indicates the consistency with which the regions participate across the 96 optimization runs. B) Same as panel A, except optimization carried out for Acc. Only one consistent pattern emerges, comprising 93 unique outcomes. Optimizations are carried out on the HCP data set (all subjects, all runs).

in training set, 5 runs in testing set; optimizing for I_{diff} only; data not shown).

Discussion

Our study aimed to leverage a temporal decomposition of eTS (Faskowitz et al. 2020; Sporns et al. 2021) to pinpoint spatiotemporal features supporting individual differences in FC with high temporal resolution at the level of individual TRs in fMRI time series. We show that the identifiability of frames differs across edge cofluctuation amplitude, across similarity with other frames in the run, and across velocity of transitions between adjacent time points. Notably, these relations differed based on the specific identifiability metric used across both the HCP and MSC data sets, showing that methods commonly used in the fingerprinting literature (differential identifiability [I_{diff}]: the average identification of subjects with themselves above the relation with others, and accuracy [Acc]: the rate of success of subject identification) display distinctive characteristics of fingerprints. Identifiability was found to be higher for high cofluctuation amplitude frames while accuracy was higher for midamplitude frames. Removing high-amplitude frames revealed that identifiability largely maps onto moments in time that drive full FC estimates while fingerprinting features that amplify accuracy map onto frames with mid- to low-amplitude and therefore may be less represented in full FC using standard methods. Furthermore, frames selected based on template patterns were consistent across both identifiability and accuracy as well as across

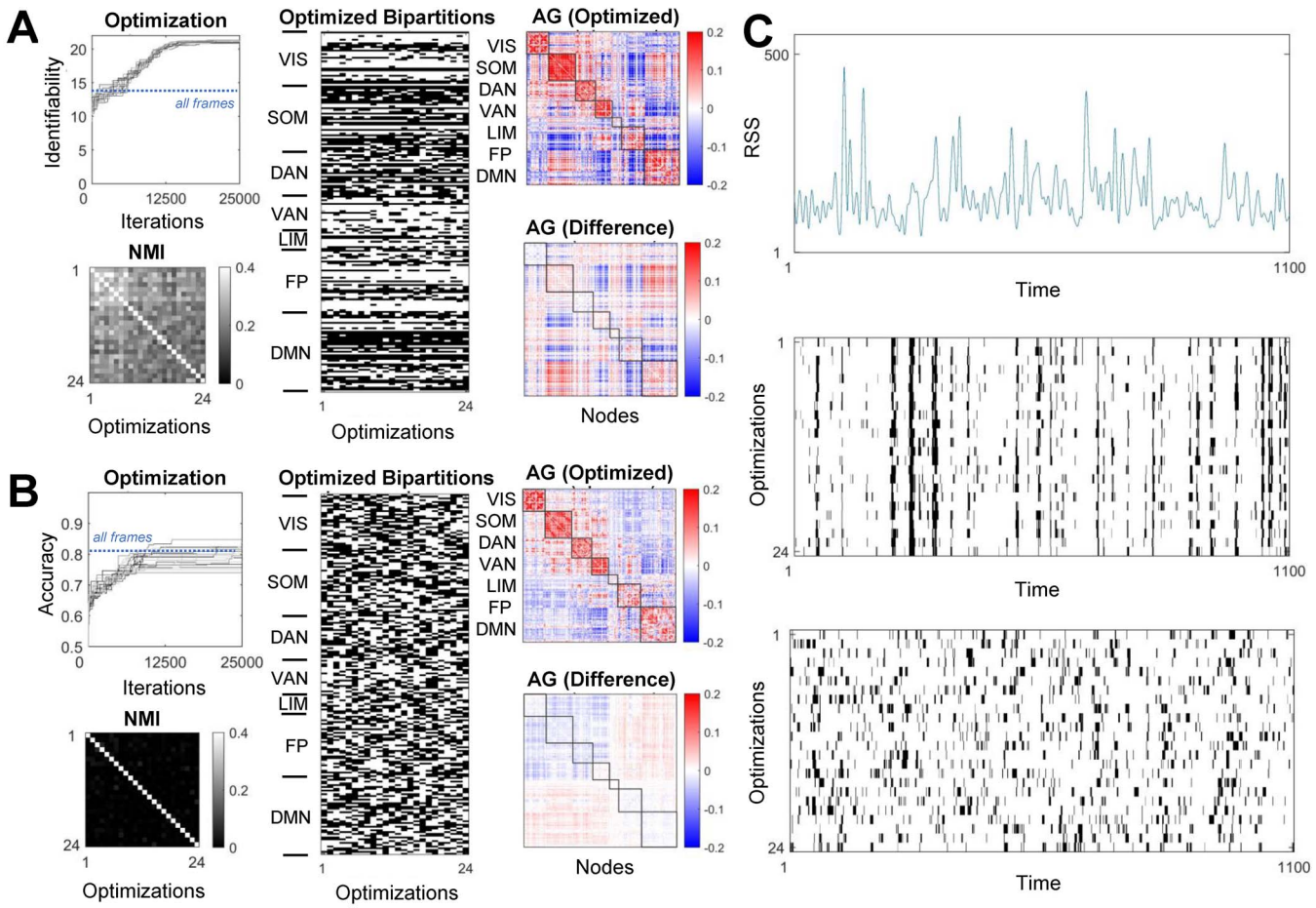

Fig. 8. Frame set optimizations. A) Optimizations for I_{diff}. B) Optimizations for Acc. (left) Evolution of the objective function for 24 optimizations (top) and their normalized mutual information (NMI, expressing their similarity). In the NMI plots, optimizations are arranged in order of quality (i.e. by the value of the objective function at the end of the run). Note that for I_{diff}, individual runs converge on a common pattern, indicated by high MI between different runs. By contrast, for Acc, no such convergence occurs. Performance level for I_{diff} and Acc when using all frames (full runs) is indicated by a blue line. (Middle) Optimized bipartitions, and topography of the mean AG component for the optimized bipartitions (averaged over all 24 runs). Top plot shows the mean optimized AG component, bottom plot shows the difference in AG components before and after optimizations. C) Selection of moments in time, for each of 24 optimizations, demonstrated for data from 1 subject, 1 run. The 3 plots show the RSS amplitude for the selected run (top), and the time points chosen for each of the 24 optimizations (middle: I_{diff}; bottom: Acc). In the optimizations for I_{diff} (middle panel), note the overlap in selected time points across 24 optimizations and the lack of a relationship of those time points with the cofluctuation amplitude (RSS). No time points are consistently selected in optimizations for Acc (bottom panel). All optimizations were carried out on HCP data (48 subjects, randomly selected as the "training set"). For transfer of fingerprinting performance to held-out subjects in the "testing set," see Supplementary Fig. S6.

data sets, showing that certain system template patterns of cofluctuations, indicative of system expression, are more predictive of subject identity than others. Lastly, we deployed an optimization strategy to detect spatial and temporal features that maximally express individual differences. We found that when optimizing based on node sets, the best solutions converged on distinct and disjunct node sets centered on either the FP or the VAN. When optimizing across time for identifiability, the optimal connectivity pattern consistently converged onto the same spatiotemporal signature (consistent moments in time). By contrast, optimizing for accuracy revealed highly distinct patterns, both in space and time, centered on moments when brain-wide cofluctuations were modest in size. These results suggest that individual frames contribute differentially to individual differences quantified with the fingerprinting metrics identifiability and accuracy and that there are multiple types of FC fingerprints embedded throughout resting-state dynamics.

Extensive past work has converged on amplified fingerprints in the FP, DMN networks, and their between-network connectivity with the attentional networks (Mira-Dominguez et al. 2014; Finn et al. 2015; Airan et al. 2016; Amico and Goñi 2018; Gratton et al. 2018; Peña-Gómez et al. 2018; Byrge and Kennedy 2019; Ravindra et al. 2021; Sareen et al. 2021). Further work outlines the modes of activity patterns attributable to the most variable or distinguishable features in FC data (Amico and Goñi 2018; Sripada et al. 2019). These efforts mainly focused on spatial subject-distinctive features from data gathered over an entire run. Our work also converges on these higher-order association areas with the additional benefit of preserving global information regarding how identifiable regions of interest relate both to other edges and time frames. Although the

specific regions have been clarified, other methods, such as point process analysis and coactivation pattern analysis, have also revealed that brief moments in time with high BOLD activation dominate RSN estimates across entire runs (Tagliazucchi et al. 2011; Caballero Gaudes et al. 2013; Liu and Duyn 2013; Allan et al. 2015; Karahanoğlu and Van De Ville 2015; Liu et al. 2018b). With our approach, these moments in time can be selected based on cofluctuations of activity between regions regardless of BOLD amplitude and without the need to consider specific seed regions. This allows us to temporally track how identifiability evolves throughout a run based on predetermined metrics of interest. In general, the compression of fMRI time series into binary format (bipartitions) yields a compact and yet rich feature set as a basis for optimization and machine learning applications.

Previous work has also explored the temporal features of FC fingerprints (Vidaurre et al. 2017; Peña-Gómez et al. 2018; Liu et al. 2018a; Van De Ville et al. 2021). However, these approaches have largely utilized FC windowing (Lurie et al. 2020), which entails methodological issues such as selection of free parameters like window sizes and spacings. Multiple efforts have now shown that brief moments in time displaying high-amplitude cofluctuations called "events" dominate FC estimates (Keilholz et al. 2017; Cifre et al. 2020; Esfahlani et al. 2020). Considering that windowing analyses are based on user-defined decisions and invariably smooth the spatial signals over many seconds (Hindriks et al. 2016; Shakil et al. 2016; Preti et al. 2017; Esfahlani et al. 2020), it remains unclear whether events also dominate multiple dynamic connectivity estimates. By contrast, our approach filters time points based on features obtained at the fine-scale single-TR native resolution of the time series, harvesting instantaneous spatial patterns at brief moments in time. Our findings show that greater levels of identifiability and accuracy can arise from moments in time outside of high-amplitude cofluctuations, even exceeding levels obtained by using the full data set (see also Amico and Goñi 2018). Since high-amplitude "events" contribute disproportionately to full nFC, our approach, as demonstrated in this study, may uncover fingerprinting features that were previously hidden from view.

Our results further show that data-driven optimization arrives at multiple sets of FC components with high or optimal identifiability and accuracy. It appears that not 1, but multiple fingerprints are contained within BOLD time series. This finding may help clarify disparate results in the literature regarding the localization of identifiable regions, with several bodies of work showing there are more identifiable regions/systems (Finn et al. 2015) and others showing that identifiability is homogenously located throughout the cortex (Byrge and Kennedy 2019). Our results suggest that identifiability may depend on the chosen metric of interest. Here, our optimization results converge on specific regions consistent with extant literature when defining patterns based on I_{diff}, while optimizing Acc results in patterns that are more variable and do not converge on consistent moments in time. In addition to past work, our method provides a framework to pinpoint moments in time when edges or specific features contribute the most toward fingerprinting. Considering that multiple patterns of activity that contribute less toward traditional FC maximize subject identifiability, even above that of standard methods, suggests that relevant features of resting-state data may remain untapped for potential brain–behavior relationships. So far, resting-state has been found to be related to task-evoked coactivation states (Cole et al. 2014) and predictive of behavioral performance (Cole et al. 2012; Rosenberg et al. 2016; Yamashita et al. 2018; Fong et al. 2019; Rosenberg et al. 2020; Sripada et al. 2020). Recently however, naturalistic stimuli (e.g. movies) and task-based FC have been shown to improve behavioral predictions in FC above resting state (Finn et al. 2017; Vanderwal et al. 2017; Greene et al. 2018; Finn and Bandettini 2021). Similarly, to selecting FC features based on improving predictions of behavioral performance (Finn and Rosenberg 2021), elucidating brain–behavior relations in resting-state data may benefit from selecting specific moments in time. Future work should determine whether fine-scale identifiability varies with task and whether different patterns of optimally identifiable or accurate patterns predict different types of behaviors.

These potentially hidden moments expressing subject-specific patterns may aid in the discovery of cognitive and clinical biomarkers not yet fully explored through analysis of full or windowed FC. Individualized features of event patterns dominate full FC (Betzel et al. 2022), implying that most extant work on full FC has focused on differences expressed during these brief moments in time. Our study suggests that signatures of individual differences exist outside of these high-amplitude frames and may yet contribute toward a greater understanding of different disorders. If specific activity patterns can be related to differences in behaviors of interest, individuals could be more readily compared across similar patterns of activity that sparsely occur within a run.

Although this work highlights additional features that optimize identifiability, the exact sources of these fingerprints remain to be identified and appear to be driven by multiple factors. Many of these differences are likely constrained by features that are stable over longer time scales such as individual variations in brain architecture (Germann et al. 2020) and resting-state functional networks (Mueller et al. 2013; Seitzman et al. 2019). Considering the brain's structural architecture can elicit patterns similar to resting-state FC (Honey et al. 2009), and that differences in structure influence alterations in communication dynamics (Seguin et al. 2020), suggests that individual variations in structure may also be indicative of natural variations in functional networks and behavior. Additionally, estimated activity flow across RSNs can be used to predict cognitive task activations (Cole et al.

2016), making individual differences in functional networks (Gordon et al. 2017; Seitzman et al. 2019) another exciting avenue for further investigation.

Several potential biases and limitations should be discussed. True estimates of structure and function are likely presently confounded by variations in stable traits such as head motion (Siegel et al. 2017), which is further heritable (Couvy-Duchesne et al. 2014), potential differences in vasculature (Golestani et al. 2016), or ability for subjects to remain alert in the scanner. We examined FD and its possible relation to RSS, as well as a potential framewise metric, but did not discover significant correlations between these metrics or motion biases in frame selection. Regardless, motion remains a concern and should be carefully controlled for in future work. In addition to motion, differences in scanner, run time, acquisition parameters, and preprocessing pipelines (Botvinik-Nezer et al. 2020) make comparisons across labs more challenging, but research continues to support real effects of fingerprinting across multiple sites (Bari et al. 2019). In our study, we compared findings across 2 data sets, HCP and MSC. A notable difference between them is the TR (HCP: 720 ms, MSC: 2,200 ms). While, as a result, autocorrelation profiles differ between the 2 data sets (Supplementary Fig. S10), basic findings are consistent. We speculate that the longer TR (reducing similarity of edge cofluctuation patterns between adjacent time points) may contribute to better performance in I_{diff} and Acc for MSC as it would tend to produce more variable frame sets. Finally, there is continuing debate on whether fMRI resting state is truly dynamic to begin with (Laumann et al. 2017; Lurie et al. 2020). Our approach provides the temporal and spatial resolution to continue to explore this issue.

Our results further emphasize the importance of choice in fingerprinting metrics. For instance, accuracy (also referred to as success rate) expresses the fraction of cases where subjects identified with themselves over others between runs. Hence, the metric is blind to the magnitude of this difference and the correlations involved. On the other hand, differential identifiability focuses on the average difference between within- versus between-subject comparisons. We find that these 2 metrics display different behaviors given the same data set, which is in line with previous work. For example, Van De Ville et al. (2021) considers dynamic identification of individuals at different time scales. They find that shorter time scales can display high levels of Acc simultaneously with near-0 I_{diff}. This would appear to indicate that Acc detects insignificant and spurious correlations in addition to larger signals. Our findings, however, suggest that Acc may be able to pick up subtle, individual-specific differences of interest, and we observe instances where I_{diff} is high while Acc is low. The relation between I_{diff} and Acc, as well as other potential fingerprinting metrics, merits further investigation.

Another important consideration is determining how various temporal filtering methods contribute toward full FC. Amico and Goñi (2018) show that multiple PCA components are necessary to improve I_{diff} beyond the levels of full FC. They find that the first few PCA components alone display lower I_{diff}, which improves when adding additional components prior to an inflection. Notably, we found that the first principal component of a set of bipartitions derived from each participant's eTS has the highest correlation with RSS (Sporns et al. 2021). This suggests convergence between Amico and Goñi (2018) and our RSS results even though RSS deciles (determined on a run-by-run basis) and PCA components (computed across all subjects) are nonidentical. Specifically, the highest RSS decile alone displays lower I_{diff} compared to full FC (Fig. 3) and high values of I_{diff} are still seen upon removal of high RSS frames (Fig. 4). This suggests that lower RSS frames (which do not contribute as strongly to full FC; Esfahlani et al. 2020) also contribute toward I_{diff}. Hence, in agreement with Amico and Goñi (2018), our work provides additional evidence that dynamic features of fingerprinting are distributed over many time points, with contributions from multiple PCA components and/or RSS bins. Further work is needed to determine the precise relationship between PCA and the temporal filtering approach adopted in our study.

Conclusion

In summary, this work reveals the existence of multiple fingerprints, in space and time, within resting-state neuroimaging data and proposes a new method for temporally filtering BOLD time series. Traditionally utilized fingerprinting metrics display distinctive characteristics that enhance distinguishable framewise features and converge on a subset of system-based templates that outperform other activity patterns. Further investigation of the patterns and origins of these individual differences in FC may support efforts toward personalized medicine as well as our understanding of behaviors that are not as well categorized by group averages and where activity cannot be solely linked to lower dimensional features of the structural network.

Supplementary material

Supplementary material is available at *Cerebral Cortex* online.

Acknowledgements

Data were provided, in part, by the HCP, WU-Minn Consortium (principal investigators: D. Van Essen and K. Ugurbil; 1U54MH091657), funded by the 16 National Institutes of Health (NIH) institutes and centers that support the NIH Blueprint for Neuroscience Research and by the McDonnell Center for Systems Neuroscience at Washington University.

Funding

This research was supported by the National Science Foundation under grant no. (NSF IIS-2023985; O.S., R.F.B.)

and by Indiana University Office of the Vice President for Research Emerging Area of Research Initiative, Learning: Brains, Machines and Children (R.F.B.).

Conflict of interest statement: None declared.

Data Availability

The two data sets used in this article are publicly available upon access request. Human Connectome Project neuroimaging data is available after signing a data use agreement at the link: https://db.humanconnectome.org/. Midnight Scan Club neuroimaging was obtained from the OpenNeuro database, with the accession number ds000224. It is openly available at the link: https://openneuro.org/datasets/ds000224/. Matlab code packages are available online for computing edge time series, bipartitions and derived measures (https://www.brainnetworkslab.com/coderesources) and for computing other graph theoretic constructs and metrics (https://sites.google.com/site/bctnet/).

References

Adelstein JS, Shehzad Z, Mennes M, DeYoung CG, Zuo XN, Kelly C, Margulies DS, Bloomfield A, Gray JR, Castellanos FX, et al. Personality is reflected in the brain's intrinsic functional architecture. *PLoS One*. 2011:6(11):e27633. https://doi.org/10.1371/journal.pone.0027633.

Airan RD, Vogelstein JT, Pillai JJ, Caffo B, Pekar JJ, Sair HI. Factors affecting characterization and localization of interindividual differences in functional connectivity using MRI. *Hum Brain Mapp*. 2016:37(5):1986–1997. https://doi.org/10.1002/hbm.23150.

Allan TW, Francis ST, Caballero-Gaudes C, Morris PG, Liddle EB, Liddle PF, Brookes MJ, Gowland PA. Functional connectivity in MRI is driven by spontaneous BOLD events. *PLoS One*. 2015:10(4):1–17. https://doi.org/10.1371/journal.pone.0124577.

Amico E, Goñi J. The quest for identifiability in human functional connectomes. *Sci Rep*. 2018:8(1):8254. https://doi.org/10.1038/s41598-018-25089-1.

Bari S, Amico E, Vike N, Talavage TM, Goñi J. Uncovering multi-site identifiability based on resting-state functional connectomes. *NeuroImage*. 2019:202(April):115967. https://doi.org/10.1016/j.neuroimage.2019.06.045.

Betzel RF, Cutts SA, Greenwell S, Faskowitz J, Sporns O. Individualized event structure drives individual differences in whole-brain functional connectivity. *NeuroImage*. 2022:252(February):118993. https://doi.org/10.1016/j.neuroimage.2022.118993.

Botvinik-Nezer R, Holzmeister F, Camerer CF, Dreber A, Huber J, Johannesson M, Kirchler M, Iwanir R, Mumford JA, Adcock RA, et al. Variability in the analysis of a single neuroimaging dataset by many teams. *Nature*. 2020:582(7810):84–88. https://doi.org/10.1038/s41586-020-2314-9.

Buckner RL, Krienen FM. The evolution of distributed association networks in the human brain. *Trends Cogn Sci*. 2013:17(12):648–665. https://doi.org/10.1016/j.tics.2013.09.017.

Byrge L, Kennedy DP. High-accuracy individual identification using a "thin slice" of the functional connectome. *Network Neurosci*. 2019:3(2):363–383. https://doi.org/10.1162/netn_a_00068.

Caballero Gaudes C, Petridou N, Francis ST, Dryden IL, Gowland PA. Paradigm free mapping with sparse regression automatically detects single-trial functional magnetic resonance imaging blood oxygenation level dependent responses. *Hum Brain Mapp*. 2013:34(3):501–518. https://doi.org/10.1002/hbm.21452.

Cabral J, Vidaurre D, Marques P, Magalhães R, Silva Moreira P, Miguel Soares J, Deco G, Sousa N, Kringelbach ML. Cognitive performance in healthy older adults relates to spontaneous switching between states of functional connectivity during rest. *Sci Rep*. 2017:7(1):1–13. https://doi.org/10.1038/s41598-017-05425-7.

Cifre I, Zarepour M, Horowitz SG, Cannas SA, Chialvo DR. Further results on why a point process is effective for estimating correlation between brain regions. *Pap Phys*. 2020:12(June):1–8. https://doi.org/10.4279/pip.120003.

Cole MW, Yarkoni T, Repovš G, Anticevic A, Braver TS. Global connectivity of prefrontal cortex predicts cognitive control and intelligence. *J Neurosci*. 2012:32(26):8988–8999. https://doi.org/10.1523/JNEUROSCI.0536-12.2012.

Cole MW, Bassett DS, Power JD, Braver TS, Petersen SE. Intrinsic and task-evoked network architectures of the human brain. *Neuron*. 2014:83(1):238–251. https://doi.org/10.1016/j.neuron.2014.05.014.

Cole MW, Ito T, Bassett DS, Schultz DH. Activity flow over resting-state networks shapes cognitive task activations. *Nature Neuroscience*. 2016:19(12):1718–1726. https://doi.org/10.1038/nn.4406.

Couvy-Duchesne B, Blokland GAM, Hickie IB, Thompson PM, Martin NG, de Zubicaray GI, McMahon KL, Wright MJ. Heritability of head motion during resting state functional MRI in 462 healthy twins. *NeuroImage*. 2014:102(P2):424–434. https://doi.org/10.1016/j.neuroimage.2014.08.010.

Dosenbach NUF, Nardos B, Cohen AL, Fair DA, Power JD, Church JA, Nelson SM, Wig GS, Vogel AC, Lessov-schlaggar CN, et al. Prediction of individual brain maturity using fMRI published by: American Association for the Advancement of Science Linked references are available on JSTOR for this article: prediction of individual brain maturity using fMRI. *Science*. 2010:329(5997):1358–1361.

Dubois J, Adolphs R. Building a science of individual differences from fMRI. *Trends Cogn Sci*. 2016:20(6):425–443. https://doi.org/10.1016/j.tics.2016.03.014.

Dubois J, Galdi P, Han Y, Paul LK, Adolphs R. Resting-state functional brain connectivity best predicts the personality dimension of openness to experience. *Personal Neurosci*. 2018a:1:e6. https://doi.org/10.1017/pen.2018.8.

Dubois J, Galdi P, Paul LK, Adolphs R. A distributed brain network predicts general intelligence from resting-state human neuroimaging data. *Philos Trans R Soc B Biol Sci*. 2018b:373(1756):20170284. https://doi.org/10.1098/rstb.2017.0284.

Elliott ML, Knodt AR, Cooke M, Kim MJ, Melzer TR, Keenan R, Ireland D, Ramrakha S, Poulton R, Caspi A, et al. General functional connectivity: shared features of resting-state and task fMRI drive reliable and heritable individual differences in functional brain networks. *NeuroImage*. 2019:189(November 2018):516–532. https://doi.org/10.1016/j.neuroimage.2019.01.068.

Emerson RW, Adams C, Nishino T, Hazlett HC, Wolff JJ, Zwaigenbaum L, Constantino JN, Shen MD, Meghan R, Elison JT, et al. Functional neuroimaging of high-risk 6-month-old infants predicts a diagnosis of autism at 24 months of age. *Sci Transl Med*. 2017:9(393):eaag2882. https://doi.org/10.1126/scitranslmed.aag2882.

Esfahlani FZ, Jo Y, Faskowitz J, Byrge L, Kennedy DP, Sporns O, Betzel RF. High-amplitude cofluctuations in cortical activity drive functional connectivity. *Proc Natl Acad Sci U S A*. 2020:117(45):28393–28401. https://doi.org/10.1073/pnas.2005531117.

Esfahlani FZ, Faskowitz J, Slack J, Mišić B, Betzel RF. Local structure-function relationships in human brain networks across the lifespan. *Nat Commun*. 2022:13(1):1–16. https://doi.org/10.1038/s41467-022-29770-y.

Esteban O, Markiewicz CJ, Blair RW, Moodie CA, Isik AI, Erramuzpe A, Gorgolewski KJ. fMRIPrep: a robust preprocessing pipeline for functional MRI. *Nature methods*. 2019:16(1):111–116. https://doi.org/10.1038/s41592-018-0235-4.

Faskowitz J, Esfahlani FZ, Jo Y, Sporns O, Betzel RF. Edge-centric functional network representations of human cerebral cortex reveal overlapping system-level architecture. *Nat Neurosci*. 2020:23(12):1644–1654. https://doi.org/10.1038/s41593-020-00719-y.

Finn ES, Bandettini PA. Movie-watching outperforms rest for functional connectivity-based prediction of behavior. *NeuroImage*. 2021:235(April):117963. https://doi.org/10.1016/j.neuroimage.2021.117963.

Finn ES, Rosenberg MD. Beyond fingerprinting: choosing predictive connectomes over reliable connectomes. *NeuroImage*. 2021:239(May):118254. https://doi.org/10.1016/j.neuroimage.2021.118254.

Finn ES, Todd Constable R. Individual variation in functional brain connectivity: implications for personalized approaches to psychiatric disease. *Dialogues Clin Neurosci*. 2016:18(3):277–287. https://doi.org/10.31887/dcns.2016.18.3/efinn.

Finn ES, Shen X, Scheinost D, Rosenberg MD, Huang J, Chun MM, Papademetris X, Constable RT. Functional connectome fingerprinting: identifying individuals using patterns of brain connectivity. *Nat Neurosci*. 2015:18(11):1664–1671. https://doi.org/10.1038/nn.4135.

Finn ES, Scheinost D, Finn DM, Shen X, Papademetris X, Constable RT. Can brain state be manipulated to emphasize individual differences in functional connectivity? *NeuroImage*. 2017:160(March):140–151. https://doi.org/10.1016/j.neuroimage.2017.03.064.

Fong AHC, Yoo K, Rosenberg MD, Zhang S, Li CSR, Scheinost D, Constable RT, Chun MM. Dynamic functional connectivity during task performance and rest predicts individual differences in attention across studies. *NeuroImage*. 2019:188(December 2018):14–25. https://doi.org/10.1016/j.neuroimage.2018.11.057.

Friston KJ. Functional and effective connectivity in neuroimaging: a synthesis. *Human brain mapping*. 1994:2(1–2):56–78. https://doi.org/10.1002/hbm.460020107.

Germann J, Chakravarty MM, Collins DL, Petrides M. Tight Coupling between Morphological Features of the Central Sulcus and Somatomotor Body Representations: A Combined Anatomical and Functional MRI Study. *Cerebral Cortex*. 2020:30(3):1843–1854. https://doi.org/10.1093/cercor/bhz208.

Glasser MF, Sotiropoulos SN, Wilson JA, Coalson TS, Fischl B, Andersson JL, Wu-Minn HCP Consortium. The minimal preprocessing pipelines for the Human Connectome Project. *Neuroimage*. 2013:80:105–124. https://doi.org/10.1016/j.neuroimage.2013.04.127.

Golestani AM, Kwinta JB, Strother SC, Khatamian YB, Chen JJ. The association between cerebrovascular reactivity and resting-state fMRI functional connectivity in healthy adults: the influence of basal carbon dioxide. *NeuroImage*. 2016:132:301–313. https://doi.org/10.1016/j.neuroimage.2016.02.051.

Gordon EM, Laumann TO, Gilmore AW, Newbold DJ, Greene DJ, Berg JJ, Ortega M, Hoyt-Drazen C, Gratton C, Sun H, et al. Precision functional mapping of individual human brains. *Neuron*. 2017:95(4):791–807.e7. https://doi.org/10.1016/j.neuron.2017.07.011.

Gratton C, Laumann TO, Nielsen AN, Greene DJ, Gordon EM, Gilmore AW, Nelson SM, Coalson RS, Snyder AZ, Schlaggar BL, et al. Functional brain networks are dominated by stable group and individual factors, not cognitive or daily variation. *Neuron*. 2018:98(2):439–452.e5. https://doi.org/10.1016/j.neuron.2018.03.035.

Gratton C, Kraus BT, Greene DJ, Gordon EM, Laumann TO, Nelson SM, Dosenbach NUF, Petersen SE. Defining individual-specific functional neuroanatomy for precision psychiatry. *Biol Psychiatry*. 2020:88(1):28–39. https://doi.org/10.1016/j.biopsych.2019.10.026.

Greene AS, Gao S, Scheinost D, Constable RT. Task-induced brain state manipulation improves prediction of individual traits. *Nat Commun*. 2018:9(1):2807. https://doi.org/10.1038/s41467-018-04920-3.

Hindriks R, Adhikari MH, Murayama Y, Ganzetti M, Mantini D, Logothetis NK, Deco G. Can sliding-window correlations reveal dynamic functional connectivity in resting-state fMRI? *NeuroImage*. 2016:127:242–256. https://doi.org/10.1016/j.neuroimage.2015.11.055.

Honey CJ, Sporns O, Cammoun L, Gigandet X, Thiran JP, Meuli R, Hagmann P. Predicting human resting-state functional connectivity from structural connectivity. *Proceedings of the National Academy of Sciences of the United States of America*. 2009:106(6):2035–2040. https://doi.org/10.1073/pnas.0811168106.

Horien C, Shen X, Scheinost D, Constable RT. The individual functional connectome is unique and stable over months to years *NeuroImage*. 2019:189:676–687. https://doi.org/10.1016/j.neuroimage.2019.02.002.

Hsu WT, Rosenberg MD, Scheinost D, Constable RT, Chun MM. Resting-state functional connectivity predicts neuroticism and extraversion in novel individuals. *Soc Cogn Affect Neurosci*. 2018:13(2):224–232. https://doi.org/10.1093/scan/nsy002.

Jalbrzikowski M, Liu F, Foran W, Klei L, Calabro FJ, Roeder K, Devlin B, Luna B. Functional connectome fingerprinting accuracy in youths and adults is similar when examined on the same day and 1.5-years apart. *Hum Brain Mapp*. 2020:41(15):4187–4199. https://doi.org/10.1002/hbm.25118.

Jeub LG, Sporns O, Fortunato S. Multiresolution consensus clustering in networks. *Scientific reports*. 2018:8(1):1–16. https://doi.org/10.1038/s41598-018-21352-7.

Jo Y, Zamani Esfahlani F, Faskowitz J, Chumin EJ, Sporns O, Betzel RF. The diversity and multiplexity of edge communities within and between brain systems. *Cell Rep*. 2021a:37(7):110032. https://doi.org/10.1016/j.celrep.2021.110032.

Jo Y, Faskowitz J, Esfahlani FZ, Sporns O, Betzel RF. Subject identification using edge-centric functional connectivity. *NeuroImage*. 2021b:238(May):118204. https://doi.org/10.1016/j.neuroimage.2021.118204.

Karahanoğlu FI, Van De Ville D. Transient brain activity disentangles fMRI resting-state dynamics in terms of spatially and temporally overlapping networks. *Nat Commun*. 2015:6(1):7751. https://doi.org/10.1038/ncomms8751.

Keilholz S, Caballero-Gaudes C, Bandettini P, Deco G, Calhoun V. Time-resolved resting-state functional magnetic resonance imaging analysis: current status, challenges, and new directions. *Brain Connect*. 2017:7(8):465–481. https://doi.org/10.1089/brain.2017.0543.

Kirkpatrick S, Gelatt CD, Vecchi MP. Optimization by simulated annealing. *Science*. 1983:220(4598):671–680. https://doi.org/10.1126/science.220.4598.671.

Lake EMR, Finn ES, Noble SM, Vanderwal T, Shen X, Rosenberg MD, Spann MN, Chun MM, Scheinost D, Constable RT. The functional brain organization of an individual allows prediction of measures

of social abilities transdiagnostically in autism and attention-deficit/hyperactivity disorder. *Biol Psychiatry*. 2019:86(4):315–326. https://doi.org/10.1016/j.biopsych.2019.02.019.

Laumann TO, Gordon EM, Adeyemo B, Snyder AZ, Joo SJ, Chen MY, Gilmore AW, McDermott KB, Nelson SM, Dosenbach NUF, et al. Functional system and areal organization of a highly sampled individual human brain. *Neuron*. 2015:87(3):657–670. https://doi.org/10.1016/j.neuron.2015.06.037.

Laumann TO, Snyder AZ, Mitra A, Gordon EM, Gratton C, Adeyemo B, Gilmore AW, Nelson SM, Berg JJ, Greene DJ, et al. On the stability of BOLD fMRI correlations. *Cereb Cortex*. 2017:27(10):4719–4732. https://doi.org/10.1093/cercor/bhw265.

Liem F, Varoquaux G, Kynast J, Beyer F, Kharabian Masouleh S, Huntenburg JM, Lampe L, Rahim M, Abraham A, Craddock RC, et al. Predicting brain-age from multimodal imaging data captures cognitive impairment. *NeuroImage*. 2017:148(July 2016):179–188. https://doi.org/10.1016/j.neuroimage.2016.11.005.

Liu X, Duyn JH. Time-varying functional network information extracted from brief instances of spontaneous brain activity. *Proc Natl Acad Sci U S A*. 2013:110(11):4392–4397. https://doi.org/10.1073/pnas.1216856110.

Liu J, Liao X, Xia M, He Y. Chronnectome fingerprinting: identifying individuals and predicting higher cognitive functions using dynamic brain connectivity patterns. *Hum Brain Mapp*. 2018a:39(2):902–915. https://doi.org/10.1002/hbm.23890.

Liu X, Zhang N, Chang C, Duyn JH. Co-activation patterns in resting-state fMRI signals. *NeuroImage*. 2018b:180(Pt B):485–494. https://doi.org/10.1016/j.neuroimage.2018.01.041.

Lurie DJ, Kessler D, Bassett DS, Betzel RF, Breakspear M, Kheilholz S, Kucyi A, Liégeois R, Lindquist MA, McIntosh AR, et al. Questions and controversies in the study of time-varying functional connectivity in resting fMRI. *Network Neurosci*. 2020:4(1):30–69. https://doi.org/10.1162/netn_a_00116.

Lynall ME, Bassett DS, Kerwin R, McKenna PJ, Kitzbichler M, Muller U, Bullmore E. Functional connectivity and brain networks in schizophrenia. *J Neurosci*. 2010:30(28):9477–9487. https://doi.org/10.1523/JNEUROSCI.0333-10.2010.

Lynch CJ, Silver BM, Dubin MJ, Martin A, Voss HU, Jones RM, Power JD. Prevalent and sex-biased breathing patterns modify functional connectivity MRI in young adults. *Nat Commun*. 2020:11(1):1–14. https://doi.org/10.1038/s41467-020-18974-9.

Metropolis N, Rosenbluth AW, Rosenbluth MN, Teller AH, Teller E. Equation of state calculations by fast computing machines. *J Chem Phys*. 1953:21(6):1087–1092. https://doi.org/10.1063/1.1699114.

Mira-Dominguez O, Mills BD, Carpenter SD, Grant KA, Kroenke CD, Nigg JT, Fair DA. Connectotyping: model based fingerprinting of the functional connectome. *PLoS One*. 2014:9(11):e111048. https://doi.org/10.1371/journal.pone.0111048.

Mueller S, Wang D, Fox MD, Yeo BTT, Sepulcre J, Sabuncu MR, Shafee R, Lu J, Liu H. Individual variability in functional connectivity architecture of the human brain. *Neuron*. 2013:77(3):586–595. https://doi.org/10.1016/j.neuron.2012.12.028.

Nielsen AN, Greene DJ, Gratton C, Dosenbach NUF, Petersen SE, Schlaggar BL. Evaluating the prediction of brain maturity from functional connectivity after motion artifact denoising. *Cereb Cortex*. 2019:29(6):2455–2469. https://doi.org/10.1093/cercor/bhy117.

Noble S, Scheinost D, Constable RT. A decade of test-retest reliability of functional connectivity: a systematic review and meta-analysis. *NeuroImage*. 2019:203(August):116157. https://doi.org/10.1016/j.neuroimage.2019.116157.

Noble S, Scheinost D, Constable RT. A guide to the measurement and interpretation of fMRI test-retest reliability. *Curr Opin Behav Sci*. 2021:40:27–32. https://doi.org/10.1016/j.cobeha.2020.12.012.

Nostro AD, Müller VI, Varikuti DP, Pläschke RN, Hoffstaedter F, Langner R, Patil KR, Eickhoff SB. Predicting personality from network-based resting-state functional connectivity. *Brain Struct Funct*. 2018:223(6):2699–2719. https://doi.org/10.1007/s00429-018-1651-z.

Power JD, Cohen AL, Nelson SM, Wig GS, Barnes KA, Church JA, Petersen SE. Functional network organization of the human brain. *Neuron*. 2011:72:665–678. https://doi.org/10.1016/j.neuron.2011.09.006.

Pannunzi M, Hindriks R, Bettinardi RG, Wenger E, Lisofsky N, Martensson J, Butler O, Filevich E, Becker M, Lochstet M, et al. Resting-state fMRI correlations: from link-wise unreliability to whole brain stability. *NeuroImage*. 2017:157(May):250–262. https://doi.org/10.1016/j.neuroimage.2017.06.006.

Parkes L, Fulcher B, Yücel M, Fornito A. An evaluation of the efficacy, reliability, and sensitivity of motion correction strategies for resting-state functional MRI. *NeuroImage*. 2018:171(July 2017):415–436. https://doi.org/10.1016/j.neuroimage.2017.12.073.

Parkes L, Satterthwaite TD, Bassett DS. Towards precise resting-state fMRI biomarkers in psychiatry: synthesizing developments in transdiagnostic research, dimensional models of psychopathology, and normative neurodevelopment. *Curr Opin Neurobiol*. 2020:65:120–128. https://doi.org/10.1016/j.conb.2020.10.016.

Peña-Gómez C, Avena-Koenigsberger A, Sepulcre J, Sporns O. Spatiotemporal network markers of individual variability in the human functional connectome. *Cereb Cortex*. 2018:28(8):2922–2934. https://doi.org/10.1093/cercor/bhx170.

Plitta M, Barnes KA, Wallace GL, Kenworthy L, Martin A. Resting-state functional connectivity predicts longitudinal change in autistic traits and adaptive functioning in autism. *Proc Natl Acad Sci U S A*. 2015:112(48):E6699–E6706. https://doi.org/10.1073/pnas.1510098112.

Power JD, Barnes KA, Snyder AZ, Schlaggar BL, Petersen SE. Spurious but systematic correlations in functional connectivity MRI networks arise from subject motion. *NeuroImage*. 2012:59(3):2142–2154. https://doi.org/10.1016/j.neuroimage.2011.10.018.

Preti MG, Bolton TA, Van De Ville D. The dynamic functional connectome: state-of-the-art and perspectives. *NeuroImage*. 2017:160(December 2016):41–54. https://doi.org/10.1016/j.neuroimage.2016.12.061.

Ravindra V, Drineas P, Grama A. Constructing compact signatures for individual fingerprinting of brain connectomes. *Front Neurosci*. 2021:15(April):1–14. https://doi.org/10.3389/fnins.2021.549322.

Rogers BP, Morgan VL, Newton AT, Gore JC. Assessing functional connectivity in the human brain by fMRI. *Magn Reson Imaging*. 2007:25(10):1347–1357. https://doi.org/10.1016/j.mri.2007.03.007.

Rosenberg MD, Finn ES, Scheinost D, Papademetris X, Shen X, Constable RT, Chun MM. A neuromarker of sustained attention from whole-brain functional connectivity. *Nat Neurosci*. 2015:19(1):165–171. https://doi.org/10.1038/nn.4179.

Rosenberg MD, Finn ES, Scheinost D, Papademetris X, Shen X, Constable RT, Chun MM. A neuromarker of sustained attention from whole-brain functional connectivity. *Nature neuroscience*. 2016:19(1):165–171. https://doi.org/10.1038/nn.4179.

Rosenberg MD, Scheinost D, Greene AS, Avery EW, Kwon YH, Finn ES, Ramani R, Qiu M, Todd Constable R, Chun MM. Functional connectivity predicts changes in attention observed across minutes, days, and months. *Proc Natl Acad Sci U S A*. 2020:117(7):3797–3807. https://doi.org/10.1073/pnas.1912226117.

Rubinov M, Sporns O. Complex network measures of brain connectivity: uses and interpretations. *NeuroImage*. 2010:52(3): 1059–1069. https://doi.org/10.1016/j.neuroimage.2009.10.003.

Salimi-Khorshidi G, Douaud G, Beckmann CF, Glasser MF, Griffanti L, Smith SM. Automatic denoising of functional MRI data: combining independent component analysis and hierarchical fusion of classifiers. *NeuroImage*. 2014:90:449–468. https://doi.org/10.1016/j.neuroimage.2013.11.046.

Sareen E, Zahar S, Ville D, Gupta A, Griffa A, Amico E. Exploring MEG brain fingerprints: evaluation, pitfalls, and interpretations. *NeuroImage*. 2021:240(June):118331. https://doi.org/10.1016/j.neuroimage.2021.118331.

Satterthwaite TD, Elliott MA, Gerraty RT, Ruparel K, Loughead J, Calkins ME, Eickhoff SB, Hakonarson H, Gur RC, Gur RE, et al. An improved framework for confound regression and filtering for control of motion artifact in the preprocessing of resting-state functional connectivity data. *NeuroImage*. 2013:64(1):240–256. https://doi.org/10.1016/j.neuroimage.2012.08.052.

Schaefer A, Kong R, Gordon EM, Laumann TO, Zuo X-N, Holmes AJ, Eickhoff SB, Yeo BTT. Local-global parcellation of the human cerebral cortex from intrinsic functional connectivity MRI. *Cereb Cortex*. 2018:28(9):3095–3114. https://doi.org/10.1093/cercor/bhx179.

Seguin C, Tian Y, Zalesky A. Network communication models improve the behavioral and functional predictive utility of the human structural connectome. *Network Neuroscience*. 2020:4(4): 980–1006. https://doi.org/10.1162/netn_a_00161.

Seitzman BA, Gratton C, Laumann TO, Gordon EM, Adeyemo B, Dworetsky A, Kraus BT, Gilmore AW, Berg JJ, Ortega M, et al. Trait-like variants in human functional brain networks. *Proc Natl Acad Sci U S A*. 2019:116(45):22851–22861. https://doi.org/10.1073/pnas.1902932116.

Shakil S, Lee CH, Keilholz SD. Evaluation of sliding window correlation performance for characterizing dynamic functional connectivity and brain states. *NeuroImage*. 2016:133:111–128. https://doi.org/10.1016/j.neuroimage.2016.02.074.

Siegel JS, Mitra A, Laumann TO, Seitzman BA, Raichle M, Corbetta M, Snyder AZ. Data quality influences observed links between functional connectivity and behavior. *Cereb Cortex*. 2017:27(9): 4492–4502. https://doi.org/10.1093/cercor/bhw253.

Sporns O, Faskowitz J, Teixeira AS, Cutts SA, Betzel RF. Dynamic expression of brain functional systems disclosed by fine-scale analysis of edge time series. *Network Neurosci*. 2021:5(2):405–433. https://doi.org/10.1162/netn_a_00182.

Sripada C, Angstadt M, Rutherford S, Kessler D, Kim Y, Yee M, Levina E. Basic units of inter-individual variation in resting state connectomes. *Sci Rep*. 2019:9(1):1900. https://doi.org/10.1038/s41598-018-38406-5.

Sripada C, Rutherford S, Angstadt M, Thompson WK, Luciana M, Weigard A, Hyde LH, Heitzeg M. Prediction of neurocognition in youth from resting state fMRI. *Mol Psychiatry*. 2020:25(12): 3413–3421. https://doi.org/10.1038/s41380-019-0481-6.

Svaldi DO, Goñi J, Abbas K, Amico E, Clark DG, Muralidharan C, Dzemidzic M, West JD, Risacher SL, Saykin AJ, et al. Optimizing differential identifiability improves connectome predictive modeling of cognitive deficits from functional connectivity in Alzheimer's disease. *Hum Brain Mapp*. 2021:42(11):3500–3516. https://doi.org/10.1002/hbm.25448.

Tagliazucchi E, Balenzuela P, Fraiman D, Montoya P, Chialvo DR. Spontaneous BOLD event triggered averages for estimating functional connectivity at resting state. *Neurosci Lett*. 2011:488(2): 158–163. https://doi.org/10.1016/j.neulet.2010.11.020.

Van De Ville D, Farouj Y, Preti MG, Liégeois R, Amico E. When makes you unique: temporality of the human brain fingerprint. *Sci Adv*. 2021:7(42):eabj0751. https://doi.org/10.1126/sciadv.abj0751.

Van Essen DC, Smith SM, Barch DM, Behrens TE, Yacoub E, Ugurbil K, Wu-Minn HCP Consortium. The WU-Minn human connectome project: an overview. *NeuroImage*. 2013:80:62–79. https://doi.org/10.1016/j.neuroimage.2013.05.041.

Vanderwal T, Eilbott J, Finn ES, Craddock RC, Turnbull A, Castellanos FX. Individual differences in functional connectivity during naturalistic viewing conditions. *NeuroImage*. 2017:157(April):521–530. https://doi.org/10.1016/j.neuroimage.2017.06.027.

Vidaurre D, Smith SM, Woolrich MW. Brain network dynamics are hierarchically organized in time. *Proc Natl Acad Sci*. 2017:114(48): 12827–12832. https://doi.org/10.1073/pnas.1705120114.

Waller L, Walter H, Kruschwitz JD, Reuter L, Müller S, Erk S, Veer IM. Evaluating the replicability, specificity, and generalizability of connectome fingerprints. *NeuroImage*. 2017:158(May):371–377. https://doi.org/10.1016/j.neuroimage.2017.07.016.

Yamashita M, Yoshihara Y, Hashimoto R, Yahata N, Ichikawa N, Sakai Y, Yamada T, Matsukawa N, Okada G, Tanaka SC, et al. A prediction model of working memory across health and psychiatric disease using whole-brain functional connectivity. *Elife*. 2018:7: 1–26. https://doi.org/10.7554/eLife.38844.

Yeo BT, Krienen FM, Sepulcre J, Sabuncu MR, Lashkari D, Hollinshead M, Roffman JL, Smoller JW, Zöllei L, Polimeni JR, et al. The organization of the human cerebral cortex estimated by intrinsic functional connectivity. *J Neurophysiol*. 2011:106(3):1125–1165. https://doi.org/10.1152/jn.00338.2011.

Zuo XN, Xu T, Milham MP. Harnessing reliability for neuroscience research. *Nat Hum Behav*. 2019:3(August):768–771. https://doi.org/10.1038/s41562-019-0655-x.